Article:

Bouchakour, M., Zhao, X., Gamboa, D. et al. (4 more authors) (Cover date: January–February 2025) Kinematics of Submarine Channels in Response to Bank Failures. Basin Research, 37 (1). e70013. ISSN 0950-091X

https://doi.org/10.1111/bre.70013

Kinematics of submarine channels in response to bank failures

Massine Bouchakour [a], Xiaoming Zhao[a, b*], Davide Gamboa[c, d], Crina Miclăuș [e, f], Adam D. McArthur[g], Shuchun Cao [h], Li Yang [h]

[a] School of Geosciences and Technology, Southwest Petroleum University, Chengdu 610500, Sichuan, China.

[b] Key Laboratory of Natural Gas Geology of Sichuan Province, Sichuan 610500, China.

[c] Departamento de Geociências, Universidade de Aveiro, 3810-193Aveiro, Portugal.

[d] Centro de Estudos do Ambiente e do Mar (CESAM), Universidade de Aveiro, 3810-193 Aveiro.

[e] Department of Geology, Alexandru Ioan Cuza University, 20A Carol I Blvd, 700505 Iași, Romania.

[f] Doctoral School of Geosciences, Alexandru Ioan Cuza University, Iași, Romania.

[g] School of Earth and Environment, University of Leeds, Leeds LS2 9JT, United Kingdom.

[h] CNOOC International Limited, Beijing, 100028, China.

***Corresponding Author**: Xiaoming Zhao, *zhxim98@163.com*

First Author: Massine Bouchakour, *bmassine@gmail.com*

1. ABSTRACT

Submarine channel systems play a crucial role in the delivery of clastic sediments, organic carbon, and pollutants across continental margins, and help define the stratigraphic architecture of deep-sea fans and their associated reservoirs. These systems generate complex lateral migration dynamics and resulting sedimentary architectures, which are often overprinted by a variety of local factors. For example, the debris from channel-wall collapses may block or restrict channel flow, thereby influencing the kinematics of stacking elements and the sinuosity of channels. Here, we investigate the responses of submarine channels to bank failures, using quantitative approaches from the Niger Delta Fulani Channel.

Using 3-D seismic data, we introduce a novel approach to interpret the structural framework of channels, referred to as the structural gradient, which quantifies the relationship between sedimentary architecture and underlying structures. Bank failure mass transport deposits (MTDs) were characterized by downstream changes of cross-sectional area and the proportion of collapsed material deposited. These parameters were used to correlate the responses of channel width, thickness, aspect ratio and lateral migration, as well as the channel planform parameters (i.e., sinuosity and meander amplitude) to the occurrence of flanking MTDs. Our results demonstrate that bank failures significantly influence channel sinuosity by causing localized swings in channel pathways, impacting the overall channel morphology and stratigraphic evolution. The relationships between all channel parameters depend on the ratios of bank failures, and locations of channel-wall failures. The combined effects of bank failure confinement and structural growth control channel element stacking patterns, resulting in vertical stacks related to compensational relationships between adjacent channel complexes. Significant confinements by MTD emplacement led to rapid channel infill linked to progressive flow relaxation promoting progressive lateral mobility. Channel migration is limited by MTD accumulation to a maximum width of 1700 m. Channel lateral shift reacts to channel-wall collapses, resulting in limited lateral mobility at regional scale. We show for the first time how the kinematics of submarine channels evolved in terms of the constrains of channel-wall collapses and active structural deformation.

2. INTRODUCTION

Submarine channel systems control the dispersal of clastic sediments, organic carbon, and pollutants across continental margins (Piper and Normark, 2001; Babonneau et al., 2002; Mulder et al., 2012; McArthur et al., 2016; Kane and Clare, 2019), and constitute the key morphological elements of deep-sea fans (Kolla et al., 2012). Sediment-gravity flows modify channels through erosion and deposition, by driving their lateral migration on the seafloor (Deptuck et al., 2003). Thereafter, these processes provide diverse architectural styles of lateral and vertical stacking patterns (Clark and Pickering, 1996; Qin et al., 2019; Tek et al., 2021; Bouchakour et al., 2022), and a wide range of responses to allogenic and autogenic factors (Jobe et al., 2015; Gong et al., 2021). On structured continental slopes, the influence of seafloor topography and mass transport deposits (MTDs) on channel pathway and termini in deep-marine environments is particularly prevalent (Prather et al., 1998; Gee and Gawthorpe, 2006; Clark and Cartwright, 2012). Understanding submarine channel migrations and their stratigraphic record is important for characterizing the spatial distributions and dimensions of sedimentary architectures and reservoir geometries (e.g., Mayall et al., 2006 and 2010; Covault et al., 2021). However, channel depositional stacking patterns are hard to predict due to their inherent randomness and influence of local factors, such as the variations in morphology of channel conduits and the depositional relief formed by internal levees or MTDs (Jobe et al., 2020; Bouchakour et al., 2023; McArthur et al., 2024).

The lateral migration of channels frequently responds to active growth structure by establishing high channel bend curvatures around seafloor deformation (Mayall et al., 2010; Covault et al., 2021; Mitchell et al., 2021a). These styles of interaction lead to stepwise shifts and meander expansion of migrating channels (Covault et al., 2019). The response of channels to this topography can be expressed by, amongst others, bend growth, development of complicated networks, avulsion events, crevasse splays and lobes (Gee and Gawthorpe, 2006; Howlett et al., 2020). Such channel segments, deflected by active folds (sensu Clark and Cartwright, 2009 and 2011), are usually characterized by sudden lateral offsets, but can be variable and unpredictable as observed with channel scouring, aggradation at late stages of migration, or development of narrow lateral accretion packages (LAPs) (Clark and Cartwright, 2011; Mayall et al., 2010; Howlett et al., 2020; Bouchakour et al., 2022 and 2023). This non-uniform response of channels to the changes of local seafloor dip further depends on the degree of levee confinement, sediment compaction, and perhaps biased data interpretation in regards of the placement of cross-sections across deflected channels (Bouchakour et al., 2023). Notably, most documented structurally influenced channels demonstrate high degrees of sinuosity when they establish weakly confined beltways, and may react in different ways when the channels are confined by landslides (e.g., Saller et al., 2012; Covault et al., 2024). Here we address the kinematics of a channel forming coeavally with deformation, characterized by a distinct confined erosional base, deflection, and bank failure accumulations.

Channel-wall collapses are frequently observed in submarine channels, and documented as MTDs – e.g., slumps, slide blocks, and megaclasts – sourced from failures of channel walls (e.g., Goodwin and Prior, 1989; Sawyer et al., 2007 and 2013; Hansen et al., 2015; Cronin et al., 2022; McArthur et al., 2024). Such bank collapses are recognized as key morphodynamic processes and geohazard for offshore infrastructure (McArthur et al., 2024). In addition to uncertainties of their triggering factors, the subsequent impacts on channelized flows remain poorly understood. MTDs can have significant influence on the evolution of submarine channels, by imposing lateral (e.g., Kneller et al., 2016; Ward et al., 2018; Bouchakour t al., 2022) and frontal confinement (e.g., Tek et al., 2021), perturbation of gravity-flows and channel backfilling (Posamentier and Kolla, 2003; Nelson et al., 2009), triggering avulsions (Ortiz-Karpf et al., 2015), enhancing lateral migration (Kneller et al., 2016; Kremer et al., 2018), and in its wake, altering channel sinuosity (Deptuck et al., 2007; Wynn et al., 2007; Nakajima et al., 2009; Covault et al., 2024). Numerous investigations of subsurface data have imaged bank collapse materials seating on channel floors (e.g., terraces, depositional mounts, knolls, megaclasts, or rotational slumps, among other elements), often representing early stages of channel infill (e.g., Peakall et al., 2000; Deptuck et al., 2003 and 2007; Mayall et al., 2006; Lamb et al., 2008; McArthur et al., 2024). Some works documented channel diversions around collapsed depositional topography of channel/canyon sidewall failures (Peakall et al., 2000; Kertzmus. 2009; Hansen et al., 2013; Masalimova et al., 2015; Corella et al., 2016). Nonetheless, to date no study has produced a quantitative analysis on the influence of MTDs on the channel depositional stacking patterns and the lateral mobility of channels across areas of active seafloor deformation.

Here we address this challenge using 3D seismic data from the Niger Delta Slope, offshore Nigeria, to assess the responses of channel kinematics to bank failures within the structural framework of the fold and thrust belt domain (Fig. 1A), focusing on the Fulani Channel (Fig. 1B). The methods of channel migration estimators (i.e., channel lateral shift) were adapted from Bouchakour et al. (2023), and used to quantify the relationships between lateral migration and vertical aggradation (i.e., stratigraphic mobility) of channel elements and complexes across areas with bank failures. This work aims to understand how channel stacking patterns responded to depositional topography of channel-wall collapses, and how this response affected deflection of channels around structures (F2, F3, and F4 defined in Bouchakour et al., 2023).

3. GEOLOGICAL SETTING

The Niger Delta Basin is located along the Gulf of Guinea in equatorial West African margin. Its offshore area has significant 3D seismic data coverage, which is used extensively in industry and academic research (e.g., Evamy et al., 1978; Doust and Omatsola, 1990; Damuth, 1994; Rowan et al., 2004; Corredor et al., 2005; Deptuck et al., 2007). The delta sedimentary system is more than 12 km thick, with its subaerial part covering an area approximatively 75000 km^2 (Doust and Omatsola, 1990). The stratigraphic successions of the Niger Delta Basin span from the Late Cretaceous to the present-day (Damuth, 1994; Rowan et al., 2004; Corredor et al., 2005). A high flux of clastic sediments was delivered and deposited in slope systems during different phases of gravity tectonism, characterized by thrust movements that commenced around 15 Ma ago (Rouby et al., 2011; Jolly et al., 2016; Pizzi et al., 2020). Three diachronous and prograding clastic formations are defined as the Akata, Agbada, and Benin Formations (Short and Stauble, 1967; Corredor et al., 2005). In the offshore area, the Agbada Formation contains submarine channel-levee systems and lobes, mass transport deposits (MTDs), and hemipelagic mudstones (Navarre et al., 2002). The prograding Niger Delta deposits underwent gravitational collapse and developed syn-depositional detachment zones (Damuth, 1994; Corredor et al., 2005; Briggs et al., 2006), which led to its structuration into five principal domains (Fig. 1A; Corredor et al., 2005). (1) The extensional domain, in the continental shelf, with growth of normal faults and generation of depocentres. (2) The mud diapir belt, in the upper continental slope, characterized by mud volcanoes, diapirs, and shale ridges. (3) The inner fold and thrust belt, outward of the upper continental slope, expressed by imbricated thrust faults and detachment folds. (4) The transitional domain, on the lower continental slope, with a large area of minor deformation propagated through detachment folds. (5) The compressional domain, which is located in the distal part of the Niger Delta. The study area lies in the outer fold and thrust belt domain (Fig. 1A), in which deposits of the Agbada Formation provide many examples of interactions between submarine channels and active structural deformation.

3.1 The Fulani Channel and other sedimentary systems of the Niger Delta

The study area covers ca. 397.5 km^2 (dashed blue line in Fig. 1B) of the "eastern" outer fold and thrust belt domain (Corredor et al., 2005). The Fulani Channel extends to the western hinges of folds F2, F3, and F4, located West of the Amaku Channel Systems (Bouchakour et al., 2023), and the Bukuma Channel System, "BCS", (Zhao et al., 2018) (Fig. 1A-C). The Fulani Channel incised into sediments of the shallow Agbada Formation above the regional marker T80 (Fig. 1C). Based on previous investigations by Zhang et al. (2018) and Bouchakour et al. (2023), marker T300 is placed above the top of the deformed deep Agbada Formation, representing the main deformation of the outer fold and thrust belt domain (Fig. 1C). This regional marker (T300) is calibrated at ca. 8.2 Ma from the biostratigraphic analyses of Fadyia and Salami (2015) and Olayiwola et al. (2017), which nearly correlates with the base of the growth strata defined by Maloney et al. (2010), and the horizon ca. 7.4 Ma in Jolly et al. (2016) – i.e., defined from Shell's biostratigraphic data (pers.com Shell Production and Development Company, Nigeria; 2011). The timespan above this horizon extends from the Upper Miocene (Tortonian) to the present-day seafloor (T0 in Fig. 1C).

Strata infilling the syncline basins defined by T300, encompassing the Amaku Channel Systems and the Fulani Channel, can reach a thickness of ca. 600 m (Fig. 1C; see also the Units 1 and 2 in Bouchakour et al., 2022). Based on regional scale 3D seismic data interpretations of (Pizzi et al., 2020; Spina and Mazzoli. 2023), the growing fold belts formed mini-basins that were the site of sediment accumulation related to the movements of overpressured shales of the Akata Formation. The structuration of anticlines across the study area and on the large scale of the Niger Delta is characterized by rapid growth from 9.5 to 7.3 Ma, followed by relatively moderate growth up to 2 Ma-Holocene, when the development of contraction structures decreased and possibly migrated southward (Pizzi et al., 2020; Spina and Mazzolli. 2023).

The outer fold and thrust belt's Pleistocene depositional systems were markedly influenced by this long-term deformation, notably across the Aga Fold (Clark and Cartwright, 2012), near the southern lobe (Jolly et al., 2016; Pizzi et al., 2020; Mitchell et al., 2021a). In the eastern outer fold and thrust belt, the Amaku Channel Systems record substantial coeval structural growth, forcing deflection of the channels (Bouchakour et al., 2022 and 2023). The Fulani Channel trends broadly N to NE (Fig. 1B), in common with other sedimentary systems of the outer fold and thrust belt domain (Jolly et al., 2016; Zhao et al., 2019; Pizzi et al., 2020). It distributed sediment perpendicular to fold axes F2, F3, and F4 (Fig. 1B), which were developing in response to shale deformation (Corredor et al., 2005; Rouby et al., 2011). The Fulani Channel is situated at the lower part of the stratigraphic Unit 3 (Fig. 1C; see descriptions of Unit 3 in Bouchakour et al., 2022). This interval is overlain by the transparent and uniform reflections of the abandonment stages within the BCS' near sea-floor deposition (Zhao et al., 2019).

4. DATA AND METHODS

4.1 Seismic data and interpretation

Three-dimensional (3-D) seismic data were gathered by China National Offshore Oil Corporation (CNOOC) from the eastern offshore Niger Delta, ranging in water depths from 1300 to 1700 m (Fig. 1A). Seismic reflection data was processed to zero phase and displayed in SEG (Society for Exploration Geophysicists) reversed polarity. The seismic amplitude reflections were highlighted using a black-white-yellow-red color legend, through a zero-crossing (white) between overlying negative amplitude trough (black loop – av. amp -3500) and underlying positive low-amplitude (yellow – av. amp 600) to high-amplitude peaks (red loop – av. amp 3500) (Fig. 1C). The data have a sample rate of 3 ms and bin spacing of 12.5 m × 12.5 m. The seismic frequency bandwidth is 5–90 Hz, with a dominant frequency of approximately 70 Hz within the study interval. The vertical resolution is approximately 6–7 m, derived from a seismic velocity of 1480 m/s for seawater and 1900 m/s for shallow sediments (Liu et al., 2013). The depth in time was measured in milliseconds (ms) of two-way- time (TWT), and calibrated using borehole data. This calibration enabled the conversion of vertical thicknesses to meters, with a vertical interval of 100 ms corresponding approximatively to 95 m (see Bouchakour et al., 2024 in press).

Seismic interpretation was applied on the basis of seismic stratigraphic methods (Payton, 1977; Vail, 1977) and 3-D seismic geomorphology (Posamentier et al., 2007) to identify the deep-water depositional patterns of the Fulani Channel. In addition to the 3-D interpretations, we utilized thirty-four seismic cross-sections perpendicular to the channel, spaced approximatively at 1 to 2.5 km apart along the channel length (See Supplementary Material Fig. 1). The high resolution of cross-sectional data reveals perceptible seismic geometries in the depositional architecture of channel elements and MTDs.

4.2 Structural gradient

Structural gradient (SG) is defined as the lateral steepness of a structural marker relative to the aggradational reflectors of the channel elements and the channel top surface (Fig. 2A). This parameter relies on a single structural marker which highlights a regionally discernable reflector within the deformed strata below, in this instance, the Fulani Channel (Figs. 1C and 2A). A straight line representing the main dip of this structural marker, extracted in areas below the axis and eastern flank of the studied channel, was used to identify the angular relationships with channel reflectors (Fig. 2A). Unlike dip maps, which primarily depict static orientations of steepness within geological features, SG illustrates the variation of channel responses to structural deformation, providing insights into the fold activity during the evolution of the channel. The structural gradient for channel C1 (SG-C1) was obtained by analyzing the topmost reflectors of the final "single" channel element (Fig. 2A). To ensure precise measurements, care was taken to avoid any impact from the erosional surface of the adjacent channel C2. The structural gradient for channel C2 (SG-C2) was measured in a similar way (Fig. 2A). Furthermore, an additional measurement was taken to characterize the structural marker with reference to the top surface of the Fulani Channel (SG-top; Fig. 2A). For minimizing biases in the analysis of SG-top, the top surface was taken at the horizontal distance between the two cross-sectional inflection points defined by the channel base (Fig. 2A). By obtaining accurate vertical thickness measurements in meters, confident calculation of the SG parameters was enabled. This helped eliminate any potential loss of information that could arise from normalizing the cross-sectional data, ensuring the reliability of the measurements.

Given the lack of high-resolution chronostratigraphic data in the study area and the limitations in using measurements of structural shortening (e.g., Jolly et al., 2016), the structural gradient parameters (SG-C1, SG-C2, and SG-top) were used as an alternative approach. By estimating the range (i.e., difference between maximum and minimum values at measurement points) formed by the plotted SG-C1, SG-C2, and SG-top, we were able to quantitatively analyze the local structural influences on the channel complexes and to interpret the variations of structural deformation across the Fulani Channel cross-sections (Fig. 1B). This method allowed us to observe the varying dip angles of seismic reflectors contained in stacked single channel elements along the studied channel to interpret the coeval structural growth during channel fill (Bouchakour et al., 2022). The selection of thirty-four cross-sectional measurements aimed to minimize uncertainties caused by the lack of aggradational reflectors resulting from variation of lithology or gas and fluid migration anomalies. The significant thickness of the Fulani Channel elements and the clear presence of internal reflectors facilitate the use of SG, as the interpreted aggradational reflectors occur at or above tuning thickness. However, it is important to note that at a seismic resolution 6 to 7 m, the data may not capture detailed observations of small-scale sedimentological dipping surfaces – e.g., channel bank bars and point bars – along with their associated lithological variations. Other uncertainties may arise from depositional compaction on top of the measured channel elements and the influence of shale dewatering.

4.3 Bank failure deposits and channel complex construction

This study quantified and compared channel wall MTDs (occurring in measurement sections 5-12, and 17-29; see Supplementary Material Fig. 1) with the morphology of adjacent channel fill deposits to examine their relationships. The measurements of their cross-sectional area perpendicular to channel orientation were especially focused at the channel base of the Fulani Channel, as these components (channel complex C1 and MTDs) are enclosed by its well defined bounding surface (Fig. 2A).

The cross-sectional area of the channel base (CA-Cb), the cross-sectional area of the MTD (CA-MTD), and the channel complex C1 (CA-C1) were assessed at each measurement point (Fig. 2B; see also the results in Supplementary Material Fig. 2). CA-MTD represents the deposits of MTDs, slumped channel walls, rotated blocks, and associated debris flows, while CA-C1 represents channel fill (Fig. 2A). CA-MTD/CA-C1 was also measured to gain a better understanding of relationship between the channel C1 and MTDs.

MTD ratio (%) refers to the amount of bank failure deposits located in the base of the Fulani Channel. It was normalized against the CA-Cb by calculating the proportion of MTD deposits to the channel base area (Fig. 2B). This helps avoid potential errors that may arise from proportional down-system increases in both CA-MTD and CA-Cb due to accommodation space development, referring to changes in channel depth and sedimentary context. This approach was adopted from “the depositional ratio”, defined by Qin et al. (2019). The channel complex C1 ratio (%) was similarly used to constrain the responses of C1 to MTD barriers. The results of MTD ratio were plotted along the channel distance (see Sec. 5.2) to interpret the effect of MTD topography on the channel migration and aggradation, as well as the planform distribution of C1 and C2.

4.4 Evaluating channel complex kinematics and planform distribution

We quantified the downstream evolution of channel complexes with regards to MTD ratio (%) and considered the structural framework of the Fulani Channel. We have used channel complex width (W), thickness (Th), and aspect ratio (W/Th) for channels C1 and C2 (Fig. 2C). Width (W) and thickness (Th) represent the maximum horizontal and vertical extent of the channel complex, respectively (Fig. 2C). Following the method proposed by Bouchakour et al. (2023), we have calculated the channel lateral shift (SH), defined as the horizontal ranges between the oldest and final channel element for C1 and C2 (Fig. 2C). This is an estimator of lateral mobility of channel elements during the evolution of the channel complex.

We utilized variance attribute maps extracted from two key horizons below the final channel elements for C1 and C2 to measure planform parameters (Fig. 2A). Sinuosity and meander amplitude were calculated for these final channel elements at the different sections of the Fulani Channel (Fig. 2D). We then focused on specific areas where MTDs are found in the channel base, consisting of 2 to 5 km long channel segments. The measured sinuosity was plotted against meander amplitude to analyze the responses to MTD ratio at each channel segment.

5. RESULTS

5.1 Geological structures

The study area contains three folds (F2, F3, and F4) located in the eastern margin of the Fulani Channel (Fig. 3A). Fold F2 shows a NE-SW axis that extends over 15 km in length (Fig. 3A), displaying a structural marker with weak topography, characterized by concordant layers beneath the Fulani Channel erosional base (Fig. 3B and C). Folds F3 and F4 are positioned in the southern part of the study area, with axes stretching up to 12 km in a WNW-ESE direction (Fig. 3A). They exhibit a relatively steep dip angle of the structural marker compared to the nearly horizontal seismic reflectors identified in the deposits of the Fulani Channel and its western margin (Figs. 3D, E, and H). The time structure map extracted at the structural marker shows that the folds F3 and F4 are associated with circular structures (Sa, Sb, Sc, Sd, Se, and Sf) characterized by diameters ranging between 0.7 and 2.25 km (Fig. 3A).

5.1.1 *Fluid migration paths*

Observation. The structures Sa, Sc, and Se are dominated by sub-vertical transparent, low amplitude, conduits which break the continuity of seismic stratigraphic surfaces (Fig. 3D, E, and G). These vertical conduits exhibit domed shapes at the structural marker, except for the structure Sa, which instead displays piled up V-shaped depressions (Fig. 3D). These depressions extend vertically in ca. 300 m interval from the structural marker to the seafloor (Fig. 3D).

Interpretation. Fluid migration paths described in the study area can be derived from a variety of fluids, such as paleo-gas migration including gas chimneys (Kilhams et al., 2011). Their associated circular shapes accompanied by depressions are likely derived from fluid escape, defining these structures as pockmarks (Iglesias et al., 2010).

5.1.2 *Mud volcanoes*

Observation. The structures Sb, Sd, and Sf show sub-conical shapes flanked by low amplitude lateral extensions thinning distally (Figs. 3E and H). They are discernable by vertical conduits of chaotic reflectors lined by upward tapering erections (Figs. 3D and H). Where they extend up to seafloor (Sb and Sf), they commonly form noticeable downward pointed high amplitude reflectors (Figs. 3D, E, F, and H).

Interpretation. The lateral extensions are interpreted as lateral mud extrusions vented from mud volcanoes associated with periodic expulsions of liquid, gases, and sediment (Dimitrov, 2002). The perched depressions on the seafloor (Sb and Sf) may represent pockmarks and crater-like features (Somoza et al., 2012). The structure Sd contains a buried mud volcano, overlain from the structural marker by fault-linked fluid escape structures, leading upward to pockmarks observed at the seafloor (Figs. 3F).

5.2 Seismic facies, depositional complexes and architectures of the Fulani Channel

Six seismic facies are described in Table 1, characterized by the properties and stratal terminations of seismic reflectors, and the external geometries of their packages. They are distinguished in the Fulani Channel (Sf1, Sf2, Sf4, Sf5, and Sf6), and in its overbank areas (Sf5). The relationships of seismic facies distributed on the bounding erosional base have allowed the distinction of two types of depositional complexes: channel complexes and bank failure deposits.

Table 1: Descriptions and interpretations of the seismic facies observed in the Fulani Channel.

Seismic facies	Properties	Description	Interpretation
Sf1- Channel elements 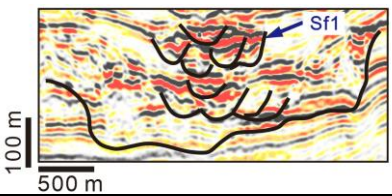	High and/or low amplitude reflectors at the tuning thickness, stacked vertically to form packages of <100 m thick, and 230-500 m wide.	Reflectors bounded by U- to V- shaped surfaces, forming sinuous pathways in planform (Fig. 4A-D).	Sand and mud prone channels, with aggradational fills confined by erosional surfaces (Deptuck et al., 2003; Gee et al., 2007 Sylvester et al., 2011).
Sf2- Internal levee 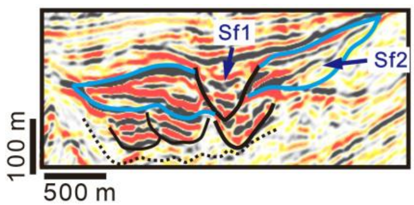	Variable amplitude reflectors, laterally continuous, tapering away from SF1. Packages of <60 m thick, and <750 m extent.	Gull-wing shaped geometry on the sides of SF1, occasionally fractured and deformed (Fig. 4A-D).	Sediments resulting from turbidity flow overspilling from the adjacent channel including mud and sands (Deptuck et al., 2003; Hansen et al., 2015 and 2017).
Sf3- External levee 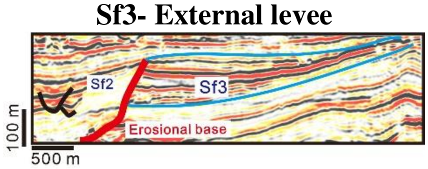	Elongated high amplitude reflectors at kilometer-scale tapering away from channel or tabular. Packages of >100 m thick.	Flat to wedge shaped geometry flanking the erosional base of the Fulani Channel (Fig. 4A-D).	External levees formed by sediment overspill dominated by coarse sand sheets (Deptuck et al., 2003; Hansen et al., 2015 and 2017).
Sf4- Rotational failure 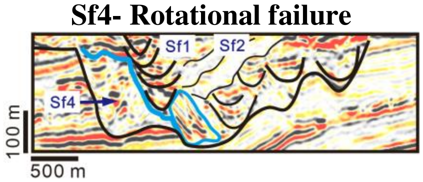	Reflectors with variable amplitudes and continuity. Packages with 200-280 thickness and 0.47-2 km width.	Fragmented and rotated packages seating on sides of the channel base of the Fulani Channel (Fig. 4A-C).	Rotational slump blocks originating from channel-wall collapses and deposited on the channel banks (Hansen et al., 2015; McArthur et al., 2024).
Sf5- Faulted failure deposits 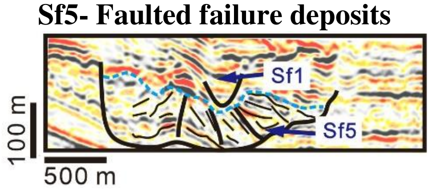	Continuous reflectors with high to moderate amplitudes constituting small packages with <58 m thickness and <120 m width.	Fractured reflectors distributed in the axis of the Fulani Channel in a close relationship with Sf4 (Fig. 4B).	Debris constituting small scale slide blocks, associated with wall-collapse fabrics (McArthur et al., 2024).
Sf6- Debris flows 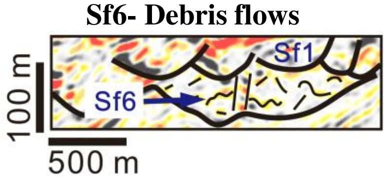	Incoherent and discontinuous low to moderate amplitude reflectors, observed with <80 m thickness and <1 km extends.	Chaotic, deformed, and fractured low to moderate amplitude reflectors distributed on the erosional base (Fig. 4A).	Debris flow "fabrics" associated with bank failures (Posamentier and Kolla, 2003; Moscardelli et al., 2006).

5.2.1 *Channel complex architecture*

Description. The channel complex architecture comprises high, low, and chaotic seismic amplitude reflector packages of channel elements (Sf1), bounded by variable amplitude reflectors of internal levees (Sf2 in Table

1, see also Figs. 4A-D). External levees bound the erosional channel basal surface, identified as high and low amplitude reflectors that converge away from the channel (Sf3 in Table 1). Two channel complexes, C1 and C2, are observed overlying this erosional base (Figs. 2A, 3B-F, and 4). These channel complexes are characterized by four types of architectures: (i) random stacking elements, coalescent U-shaped high and low amplitude reflectors, typically recognized in channel C2 (Figs. 3D and 4A); (ii) vertical stacking elements, U-shaped high amplitude reflectors, essentially edged by low amplitude to chaotic packages of Sf2 and Sf4 (Fig. 3C, E, 4B and Sf4 in Table 1); (iii) oblique stacking elements, U-shaped variable amplitude reflectors recognized in channels C1 and C2, mostly bounded by Sf4 (Fig. 3H and 4C); and (iv) lateral stacking elements, U-shaped variable amplitude reflectors recognized in channel C1 (Fig. 3D and 4D).

Interpretation. The channel complex is characterized by C1 and C2, which are of similar dimensions to the channel complexes in Sprague et al. (2005), the lateral accretion packages (LAPs - ca. <2 km width; ca. >40 m thickness) of Abreu et al. (2003), and the 4th order channels (2.2-3 km width; 50-75 m thickness) of Mayall et al (2006). While the average measured channel widths are comparable (ca. 1.28 km C1, and 1.15 km C2), the thicknesses are greater (ca. 120 m for C1, and ca. 127 m for C2). In contrast, the LAPs reported by Li and Gong, (2016) typically show smaller channel elements, ranging from ca. 40 to ca. 50 m thick. These dimensions are proportionate to outcropping submarine channel complexes of the Karoo Basin in South Africa (Pringle et al., 2010; Hodgson et al., 2011). In this study, the architectures formed by channel elements (Sf1) include: (i) irregularly arranged channel elements with frequent underscoring (McHargue et al., 2011); (ii) aggradational channel elements (Deptuck et al., 2003, Sylvester et al., 2011), usually confined by internal levees or slide blocks; (iii) migrational-aggradational channel elements (Deptuck et al., 2007; Kolla et al., 2012); and (iv) lateral migration of channel elements with cut-fill patterns (Deptuck et al., 2003 and 2007).

5.2.2 *Bank failure mass-transport deposits*

Description. Bank failure MTDs comprise three seismic facies (Table 1), constituting fragmented and rotated packages with variable shape and amplitudes of seismic reflectors (Sf4), faulted small packages with high to moderate amplitude reflectors (Sf5), and chaotic low to moderate amplitude reflectors (Sf6). Sf4 constitutes regular to slightly rotated amplitude reflectors (Figs. 3A, 4B, 5B-C, and Table 1) or dominantly discontinuous to chaotic low amplitude reflectors (Figs. 3C, 3D, and 4A). these packages overly the channel banks and are usually associated with Sf5 and Sf6 which accumulate on the axis of the Fulani Channel erosional base (Fig. 4A and Table 1).

Interpretation. Bank failure MTDs of the Fulani Channel include remobilized sediments (i.e., rotational failure-Sf4), rotating towards the channel axis then transported in proximal areas on the channel conduits (Hansen et al., 2015). The occurrence of dispersed faulted failure deposits (Sf5) and debris flows (Sf6) which are distributed on the axis of the Fulani Channel may have been sourced from the bank collapse events and deposited on the axis channel conduit (Hansen et al., 2015; McArthur et al., 2024).

5.3 Description of the Fulani Channel

5.3.1 Distribution of the Fulani Channel and interaction with structural deformation

The variance attribute map extracted below the C1's final channel element displays two main trunks of the Fulani Channel, including a relatively straight northern section in the north, referred to as the upstream channel trunk, and a large channel bend section in the south, identified as the downstream channel trunk (Fig. 5A). The studied length of the Fulani Channel is 40.5 km, as measured from the centerline of the channel base (gray dashed points in Supplementary Material Fig. 1B). The upstream channel trunk is 18.78 km long, including an NE-SW diverted segment that extends slightly away from the folds (Figs. 1B and 5A), with a channel distance ranging from 14 to 18.78 km before transitioning to the downstream channel trunk (Fig. 5A). The downstream channel trunk persists for a distance of 21.81 km (Fig. 5A), around the folds and their associated structures (Fig. 1B). The channel base has notably larger area in the downstream channel trunk (see CA-Cb averages in Supplementary Material Fig. 2). The eastern internal levees (Sf2 in Table 1) are typically constrained by the structure and show upward rotations of seismic reflectors (Fig. 5C). These levees contain a series of detachment surfaces and debris flow deposits (Sf6), flanking the structural highs of the study area. Interestingly, similar debris flow deposits progress to the channel axis near U4" (See Section 5.4 and Fig. 5A).

5.3.2 Down-system variation of the structural gradient

One striking aspect of the structural gradient SG-C1, SG-C2 and SG-top is the modifications that occurred in the downstream channel trunk during the formation of C1 and C2, and the top surface (Fig. 6), while in the sector of upstream channel trunk they are remarkably consistent, ranging from 2 to 11º, with average values of 6.25, 6.73, and 6.98º, respectively (Fig. 6). There are distinct increases of the measured structural gradients in the transition pathway to the downstream channel trunk, where SG-top is particularly high, with 17º (Fig. 6). The most significant increases of the structural gradients, reaching the highest values in the study area (Fig. 6), are related with the interaction of channel with mud volcanoes. In the downstream channel trunk, the lower value of SG-C1 indicates consistent structural growth during the development of C1 and C2 (Fig. 6).

To explore the local influence of coeval structural deformation, specifically along the downstream channel trunk, we plotted a straight line chart of SG range variations along key locations of the studied channel (Fig. 6). The values show an increasing trend from the upstream segment through the transition to the downstream channel trunk, with the highest value (8.39º) at the interaction with structures (Fig. 6). In addition, at 20 km distance along the channel, SG range has the maximum value, 21.9º. These results indicate the influence of the growing structural highs on the Fulani Channel. Active structural growth can also progressively tilt channel elements as shown in the east of the study area (Bouchakour et al., 2022).

5.4 Quantifying mass transport deposits-bank failures and controls on channel deposition

Changes in the ratio of MTDs along the channel are apparent (Fig. 7A). Distinctive accumulation of MTDs range from >20% to ca. 60%, with extent along the channel from 1.5 to 4 km (Fig. 7A). These MTD ratios correspond to bank failure accumulations at the channel base (Figs. 5A and 7A). Seven distinct MTD units were identified, including U1, U2*, U3, U4", U5, and U7*. Most of these units form rotated blocks (see Sf4 in Table 1) at the western margin (U1, U3, U4", U5, and U6; see Fig. 5A). Where rotated failure (Sf4) and faulted failure deposits (Sf5) are absent, the MTD ratio does not exceed 20%. For instance, in the southernmost downstream bend, the debris flow deposits (Sf6) have a low MTD ratio of approximatively 18%

(Fig. 7A). Where the MTD units occur on both margins on the bounding surface of Fulani Channel, U2* in the upstream and U7* in the downstream channel trunk, they represent the greatest ratios recorded for each channel transect, with 40.12% and 61.20%, respectively (Fig. 7A). Smaller ratios are observed at the upstream channel trunk in U1 (25.8%) and U3 (39.8%) as well as in the downstream transect, in sections where U4”, U5, and U6 extend with ratios 35.1, 33.7, and 51.19%, respectively. Cross-sectional data indicate that bank failure MTDs in the upstream channel trunk show pronounced ridges and rotations (Figs. 5B and 7A), showing dark packages in the variance attribute map (Fig. 5A). However, at the downstream channel trunk, they rather have flatter surfaces (except U5; Figs. 5C and 7) and occur as a distinct series of smooth and slightly fractured packages at the western margin (Fig. 5A). The MTD ratio does not reflect MTD volumes and cross-sectional areas (CA-MTD), but the relationships with the cross-section of the channel base (Section 4.3). For example, although U6 shows a significant culmination (51.19%), the CA-MTD is only 200 km^2, significantly smaller than U2* (40%) and U7* (61%), having >300 km^2 (Supplementary Material Fig. 2A). This is attributed to the narrow channel base “container”, with a CA-Cb of approximatively 400 km^2 with -188 km^2 below its average (Supplementary Material Fig. 2A).

Channel C1 shows distinct responses in relation to the MTD ratio, sharply decreasing at interactions with U1, U2*, U6, and U7* (Fig. 7B). Conversely, where C1 no longer interacts with MTD-bank failures downstream (33-38 km along channel distance; Fig. 7B), the measured ratio sharply increases to approximatively 78% and remains above 30% along the downstream bend transect. In the upstream channel trunk, C1 ratio is generally consistent ranging from approximatively 22.88 to 67.2% (Fig. 7B). However, in the downstream channel trunk, the C1 ratio covers a larger range, varying from 16.6 to 81.25% (Fig.7B). There are ambiguous relationships of C1 ratio with U4” and U5. At 19-26 km along channel distance, SG-C1 shows a positive correlation with an increase in MTD ratio from 32.38 to 50.68% (Figs. 6 and 7B). This correlation is also reflected in the development of CA-C1 (Supplementary Material Fig. 2B).

CA-MTD/CA-C1 (Fig. 7B), exhibits dominant peaks in cases of channel interaction with MTD ratios >40%, particularly U2*, U6, and U7*. It is evident that the highest occur for both channel transects, particularly where MTDs are distributed at both channel margins (U2* and U7*; Figs. 7B and 5A). CA-

MTD/CA-C1 has an inverse relationship with the measured ratio of C1, except at U4" and U5 where SG-C1 sharply increases through +25 ° along 7 km (from 5º to >30º; Fig. 6). The variations of parameters indicate they were sensitive to MTD units in Cb as well as to deformation of the underlying structural marker.

5.5 Kinematics of channel complexes and planform geometry

We plotted the width (C1-W and C2-W) and lateral shift (C1-SH and C2-SH) for each channel complex along the channel axis to analyze their responses to MTD accumulation (Fig. 8A). In the upstream channel trunk, MTD ratios exceeding 30% (U2* and U3) lead to width decreases. However, at 25.8% MTD ratio (U1) channels show width increases >1500 m, suggesting that U1 is not an efficient barrier (Fig. 8A). Among the upstream channel trunk MTD units, the sharpest width decrease occurs at a 40.12% MTD ratio (U2*), where C1-W reaches approximatively 550 m (Fig. 8A). A significant narrowing is observed at 39.8% MTD ratio (U3), with C2-W recording its lowest values in the upstream channel trunk at approximatively 750 m. In the downstream channel trunk, C1-W and C2-W also display similar patterns, except at the interaction with U5 (Fig. 8A). In this area, the interaction with dominant structural gradient (SG-C1, C2, and top: >30º, from 23 to 27 km; see Fig. 6) correlates with an increasing accumulation of CA-MTD and CA-C1 (see Supplementary Material Fig. 2B). C2 is consistently narrowed due to its compensational relationships with these older elements (Fig. 8A). As a result, the interaction with U5 (33.77%) leads to an exceptional increase in C1-W and decrease in C2-W. A 51.19% MTD ratio (U6) significantly affects C1-W, causing a sharp decrease to approximatively 1100 m, while no response is observed in C2-W. The sharpest decreases in channel complex widths occur at a 61.20% MTD ratio (U7*), reducing C1 and C2 to approximatively 500 m. However, in areas where bank failure MTDs are absent, at the downstream bend, the widths increased, reaching their maximum ranges (approximatively C1-W: 3500 m, and C2-W: 2300 m).

Channel complex thicknesses (C1-Th and C2-Th) range from 60 to 175 m in the upstream channel trunk, and from 70 to 180 m in the downstream channel trunk (Fig. 8B). They show weak sensitivity to the MTD ratio and do not exhibit any specific assortment around the structural high (i.e., the downstream channel trunk). The only noticeable response in the upstream channel trunk is observed at 39.8% MTD ratio (U3), where channel complexes slightly thicken to approximatively 125 m. Interestingly, C1-Th does not show significant sensitivity to the dominant MTD ratios of different units. However, there are distinctive increases (to around 120 and 155 m) at 20% MTD ratios around U3 and U5, respectively. In contrast, C2-Th manifests particular response to the dominant ratios of U3, U4”, and U5 (Fig. 8B). Thicknesses exceeding 180 m indicate zones of local vertical aggradation of the channel elements, at MTD ratios of 33.77% (U5) and 61.20 % (U7*).

The aspect ratio (W/Th) of channel complexes align well with the downstream changes of channel complex width and lateral shift (Fig. 8C and A). This indicates that the lateral migration of channel elements is the primary factor influencing the cross-sectional dimensions. Similar to width variations, higher MTD ratios (40.12% at U2* and 61.20% at U7*) lead to the most significant declines in W/Th, particularly for channel complex C1 (Figs. 5B-C and 8C). Within the different ranges of W/Th, the stacking patterns of C1 are dominantly oblique at the upstream channel trunk (Figs. 3B-C and 8; see also Supplementary Material, Fig. 3A-C). C2 displays random stacking patterns, becoming oblique at U2*, then vertical stacks across U3. The interaction of channel with structures results in consistent lateral stacking of C1 elements around U4”, U5, and U6. At the maximum MTD ratio 61.20% (U7*), C1 elements become aggradational. Channel complex C2 shows random stacking at U4” and predominantly oblique stacking at U7*. However, C2 develops vertically stacked elements along U5 and U6 due to compensational relationship with C1 and MTD (Fig. 8A). It is evident that where the channel complex C1 is unconfined by MTD bank collapses, it shows dominant lateral stacking patterns of its channel elements (Fig. 8C). Whereas, the channel elements of the channel complex C2 mostly tend towards oblique trajectories, likely due to the bounding levee confinement (Fig. 4B-D).

Figure 9A presents the distribution of the final channel elements for C1 and C2 and their interactions with MTD units. In the upstream channel trunk, segments U1 and U2*, which feature locally extended MTD, show a decrease in sinuosity from C1 to C2 (Fig. 9). The sinuosity and meander amplitude measurements for each channel are the highest values of the study area (Fig. 9). However, there is an exception for C2, which exhibits high sinuosity (1.12) at the U5 segment. At this segment, C2 demonstrates compensational relationships with C1 (Fig. 8; see also Supplementary Material Fig. 3E) and tends to follow similar distributions as C1 (Fig. 9A-B). At the downstream channel trunk, C1 and C2 pathways align with similar morphologies with lower ranges of sinuosity and meander amplitudes. Likely due to the influence of the locally distributed rotated blocks of U1 and U2*, C1 has greater sinuosity in the upstream channel trunk (1.55), but the measured meander amplitude (3.08 km) is more significant in the downstream channel trunk. Due to the lack of confinement by MTDs, C2 shows higher sensitivity to the structural influence with a greater sinuosity of 1.20 and greater meander amplitude of 3.09 km in the downstream channel trunk (Fig. 9B).

A plot of sinuosity against meander amplitude allows us to present the controls of MTD-channel depositional ratios on the planform distribution of the final channel elements of C1 and C2 (Fig. 10). The results show a linear increase of sinuosity and meander amplitude relative to the MTD ratios. In segments of dispersed MTDs at both channel margins (red dotted circles in Fig. 10), 61% MTD ratio (U7*) provides channel segment with lower sinuosity and amplitude, as compared with 40% (U2*). A similar signature is observed for segments where rotated failures sit on one channel margin, being ordered as follow: 51%, 41%, 34%, and 25% (Fig. 10). However, the segment U4" has anomalously low values of sinuosity and meander amplitude, likely due to the effect of debris flow and slide block accumulations in the channel axis. Overall, the plots show that the upstream channel trunk has stronger linear relationships of sinuosity and meander amplitude (0.8 against 0.5) and develop higher ranges than the downstream channel trunk. We also observe that the closer cross plot points of the southwen channel section are representative for homogenous pathways of C1 and C2 and typical compensational relationships at U5 and U6 (Fig. 10).

6. DISCUSSION

6.1 Controls of bank failures on meandering and stratigraphic evolution of channel complexes

The results demonstrate that channel complexes have developed specific signatures of cross-sectional parameters and planform morphologies at interactions with preserved deposits of channel failures. Channel complex width, lateral shift, aspect ratio, and depositional ratio vary in accordance with the accumulation of materials derived from channel wall-failures (Figs. 7 and 8). Nevertheless, channel segments traversing critical deformation of the structural marker (i.e., high SG values) show different signatures where they interact with MTDs (Figs. 6-8). In addition to the influence of MTD accumulation ratios, the planform geometries of final channel elements are also controlled by the emplacement of wall-collapses, which are distributed across the channel base (Fig. 9). Studies of submarine channels have demonstrated the implications of levee/wall-collapses on modification of channel confinement height and stratigraphic fill (e.g., Mayall et al., 2006; Sawyer et al., 2013; Hansen et al., 2015; Bouchakour et al., 2022; McArthur et al., 2024). Here, using these data integrated with channel element stacking patterns, we test if similar confinement is produced and how local sidewall failures shape the whole stratigraphic architectures of channel system.

The resulting topography of channel-bank failures influences the way that sinuosity of a channel complex develops. We show that channel segments of highest sinuosity coincide with local MTDs (Fig. 9). Where channel wall failures resulted in low MTD ratios (25%), such is the case of U1, the channel segment underwent significant bend expansion (>2 km amplitude), reflecting solid alignments of channel width, lateral shift, and aspect ratio increase with the highest sinuosity (1.85) and meander amplitude of >2 km (Figs. 7-9). This consolidation of parameters represents the development of a meandering channel (C1's youngest channel element) followed by a straight segment (C2's youngest channel element) (Fig. 9). The development of meanders in C1 is attributed to unconfined conditions resulting from the removal of channel walls and the establishment of a wide channel base. Similar style was produced by channel incisions with "rotated" and "subsided" blocks in the Benin-major Canyon (>1 km amplitude in Fig. 10 of Deptuck et al., 2007), and the "slump deposits" at the Valley-fill complex III (<1 km in Fig. 17 of Janocko et al., 2013). High sinuosity is also produced at high MTD ratio (>40%), where channel swings in confined conditions, distributed around the collapsed and rotated blocks of U2*, here instead showing decreased trends of the cross-sectional parameters (Fig. 9). Nevertheless, most studied MTD units enhanced straight channel segments (U3, 4", 5, 6, and 7*; Fig. 9). Similar channels constrained by wall-collapses are commonly observed in other settings – e.g., at the slump dominated slopes of the Monterey Canyon (see Fig. 5 in Smith et al., 2005), Espirito Santo

Basin (see Fig. 10 in Qin et al., 2016), and Miazzo, Vilafranca, and Niceto channels of the Gioia Basin (Gamberi and Rovere, 2011).

Our data show how channel wall failures may guide the evolution of channel complex cross-sectional architectures and planforms. Where MTDs are distributed on one side of channel, partial channel infill is promoted, thereafter controlling confinement. This effect is demonstrated in channel C2 by dominant aggradational stacking patterns (U3, 5, and 6; see Fig. 8C). However, the extreme confinements of wall-collapses at both channel margins may lead to very fast partial fill (e.g., Klaucke et al., 1998), causing aggradation at the channel base with vertical stacking channel elements, such as seen in C1. The subsequent sedimentary patterns within C2 reflecting oblique stacking channel elements in relatively unconfined conditions, suggests flow relaxation during the evolution of the Fulani Channel (Fig. 8C and Supplementary Material Fig. 3). In general, the stratigraphic evolution of channel pathways reveals a decrease of sinuosity from C1 to C2. However, the highest MTD ratios (at U2* and 7*) with cumulative fill at the channel base induced a divergent migration of the youngest channel element of the channel complex C2 compared to the one of the channel complex C1. These observations suggest that the material introduced by wall-collapses plays a pivotal role on the compensation relationships of channel complexes. Clark and Cartwright. (2012) reported that, in the Niger Delta outer fold and thrust belt domain, around the Aga Fold, compensational relationships between weakly confined submarine channels and MTDs drove the development of successive large bends of the channel CLS3, with meander amplitudes ranging from 2 to 3.5 km (See their Fig. 9). In this study, the channel complex C2 is much more laterally constrained (i.e., meander amplitudes of its youngest channel element are <1 km) due to the stratigraphic control of terraced topography resulting from bank failure MTDs on a deeply-incisional erosional base (Figs. 6A and Supplementary Material Fig. 3).

The accumulations of bank failures on the basal surface of the Fulani Channel at various points along its channel belt regulated the distribution of channel complexes and the evolution of architectural elements. The collapsed and excavated channel-derived elements (i.e., slide blocks and debris flow deposits) dictate how cross-sectional parameters relate with the sinuosity of the final channel elements and guide channels juxtaposition. Their influence on C1 deposition conveys subsequent stratigraphic controls on C2 architectures and distribution (Figs. 9 and 10).

6.2 How do channel bank failures constrain channel lateral migration?

A full understanding of channel kinematics, curvature, and their interactions with wall/levee failures, as well as how this depositional topography can limit lateral migration has remained elusive (Nakajima et al., 1998; Deptuck et al., 2003; Mayall et al., 2006; Deptuck et al., 2007; Sawyer et al., 2013; Saller et al., 2012; McArthur et al., 2024). The results presented here suggest that channel complexes at various stratigraphic levels respond to the MTD ratios generated by bank failures and their associated fabrics placed on the bounding basal surface of the Fulani Channel. Regardless of the structural context – i.e., at the upstream and downstream channel trunks – the presence of channel-wall collapses imposes a threshold in channel migration up to ca. 1700 m in complex width (Fig. 11). The channel migration, despite developing around active folds and structures (Fig. 5), was restricted to a width of <900 m, primarily in response to the highest ratios of MTD (>60%). Channel complexes can expand laterally to widths exceeding 1 km, but only when MTD ratios decrease, allowing for lower quantities of bank failure MTDs and creating additional accommodation for lateral channel growth. It is worth noting that the migration of channel C2 elements was directly influenced by the topography of the internal levees and the incision of channel complex C2 (Fig. 3). However, these levees and the migration of C2 elements are overridden by earlier MTD emplacement and their interaction with channel complex C1. For instance, there is clear evidence that the lateral migration of C2 elements were either obstructed or redirected by levee relief situated above the bank failure MTDs (Figs. 3B, D, E, and 9A).

One question that arises is if these channel failure events restrain or facilitate lateral migrations by removing channel wall confinement. The documented wall-collapses played a consistent role on getting greater cross-sectional areas of the channel base (CA-MTD and CA-Cb plots; see Supplementary Material Fig. 2A). The distinct lowest MTD ratios per unit (U1: >20%) seems to enhance C1 lateral migration through a typical meander expansion towards the MTDs, as well as an intercalated downstream width increase of C2 (Figs. 8A and C). Migration expansion can also be detected at MTD ratios of ca. 20% in U5, where C1 reaches similar ranges of width up to 1750 m (Fig. 8A). These data seem to reflect the consequences of early instability of the channel base providing vertical incisions within the collapsed zone that subsequently capture the migration of channel elements (e.g., Deptuck et al., 2007; Saller et al., 2012). An alternative scenario would be seen as a result of simultaneous breaching caused by the lateral meander growth (e.g., Peakall et al., 2000; Abreu et al., 2003; Deptuck et al., 2003). In contrast to facilitating the lateral migration, our data show that higher MTD ratios (>30% to >60%) are clearly responsible for limiting lateral migration. The lateral migration constraints also result in a switch in architectural styles from lateral offsets to oblique stacks within the contact of MTDs (see section 21 in Fig. 8A). In contrast, the dispersed slide blocks with debris flow deposits in the channel axis did not prevent lateral stacking patterns (Figs. 7 and 8C), leading to moderate channel sinuosity and meander amplitude values (see U4" in Fig. 10).

This work documents new insights into the evolution of submarine channels that are structurally influenced by seafloor deformation. Previously investigated deflected channels around active structural highs were often associated with an increased lateral migration and curvature towards topographic lows (e.g., Clark and Cartwright, 2009 and 2011; Mitchell et al., 2021a). However, observations of modern submarine channel systems, such as the Aldarax channel in Almeria Canyon, reveal how changing gradients influence meandering channels and effect overbank settings, including fault movements, slumping, and bank erosion (Cronin et al., 1995). Here, the Fulani Channel's downstream channel trunk represents a large meander reaching amplitude of >3 km, greater than the upstream counterpart, +1 km amplitude (Figs. 9B and 10). Whereas, the observation is that this structurally forced bend is less sinuous than the unstructured upstream channel trunk (Fig. 9B), testifying that the distributions and accumulations of channel margin collapses play a significant role on channel meandering. There is also evidence that channel complexes can only exceed the threshold of ca. 1700m width where wall-collapses are absent, allowing lateral width expansions up to 3400 m (Fig. 11A). This documented deflected bend has dominantly lateral offsets, especially along channel C1, in spite of the frequent lateral constrains of MTDs. This dominance of lateral offsets and a large bend around growing structures aligns with previously documented deflected channels (e.g., Cronin et al., 1995; Gee and Gawthorpe, 2006; Mayall et al., 2010; Clark and Cartwright, 2009, 2011; Oluboyo et al., 2014; Jolly et al., 2016; Howlett et al., 2020). However, a recent study on deflected bends demonstrated that the cross-sectional architectures are intensively modified by the confinement conditions of internal and external levee walls (Bouchakour et al., 2023). Our data here show that channel-wall collapse material can also force a vertical trajectory around a deflected channel through different conditions: (1) direct interaction with the bank failure MTDs (U7*; Figs. 8B and C); and (2) subsequent stratigraphic compensation via levee confinement (U3, 5 and 6; Figs. 8A-C).

Despite the lack of sediment supply or detailed chronostratigraphic data for the Fulani Channel, our quantitative approach allows the characterization of the down-system variations of channel kinematics and a better understanding of what causes lateral migration events. The structural gradients (SG) and their resulting ranges suggest that active deformation and diversion of channel around structures led to large channel meander but the sinuosity of this deflected bend (i.e., downstream channel trunk) was mostly dependent on the wall-collapses (Fig. 9B). Another key observation is that the MTD ratios impose limits on channel lateral migration, via channel complex widths, without any impact of their stratigraphic positions or structural responses.

6.3 Comparison to other structurally influenced and non-structured submarine channel systems

The data compiled for the Fulani Channel was compared with data sets of submarine channel systems, which are structurally deflected (Prather, 2003; Clark and Cartwright, 2011; Howlett et al., 2020; Mitchell et al., 2021b; Covault et al., 2021; Bouchakour et al., 2023) and non-structurally influenced (Abreu et al., 2003; Posamentier, 2003; Posamentier and Kolla, 2003; Kolla et al., 2012; Saller et al., 2012; McArthur and Tek, 2021; Tek et al., 2021). This comparison allows us to better understand the context of channel bank failures controls on lateral migration.

The main result of this study is that the Fulani Channel, driven by channel-wall collapses, significantly differs from most of other structurally influenced channels (SH; Fig. 11B). Whereas, similarities can be found with the Amaku Channel Systems (SH – Q3 <1000 m), where external and internal levees may play a similar role to hamper the structural controls on channel migration (Bouchakour et al., 2023). We surmise that due to their geographical proximities with the Fulani Channel, this limited lateral shift development can result in part from unknown regional factors (e.g., sediment supply, sediment transfer in the shelf edge/canyons, and large scale configuration of the Niger Delta's intra-slope basins). However, our detailed seismic interpretations along each of these channels allow us to confirm that confinement from wall-collapses (in this study) and levee heights represent the main factors that constrain lateral shifts (Bouchakour et al., 2022 and 2023). The SH mean of the documented channel nearly falls within the one of the salt influenced channels of the Kwanza and Levant Basins (Clark and Cartwright, 2011; Howlett et al., 2020). However, the channel complexes in the latter basin were able to extend laterally in greater distances (SH – Q3 >1000m; Fig. 11B), as far as they are limited by their outer levee walls enhancing a "hockey-stick" shaped architectures of channel elements at the Levant Basin (Clark and Cartwright, 2011), or a limit introduced by both levees and underlying salt-cored structures of the Kwanza Basin (Howlett et al., 2020). Without significant depositional confinements of levees, as the case of the ponded fans of prograding slope aprons (Fig. 12 in Prather, 2003) and the spectacular deflections of channel complexes documented in Mayall et al (2010), the lateral migrations can take place with larger ranges (SH – Q3 > 2000 m to ca. 4000 m; Fig. 11B). The "un-leveed channels" of the Campos Basin were able to migrate regionally across salt diapirs (Covault et al., 2021), at a basin scale extension to reach SH – Q3 > 8 km (Fig. 11B), in stark contrast with the Fulani Channel dominated by wall-collapses.

Nevertheless, even the non-structured channels can surpass the migrations of the Fulani Channel (Fig. 11B). The East Kalimantan channels of offshore Indonesia (Posamentier and Kolla, 2003; Saller et al., 2012) and the Joshua Channel (Posamentier, 2003), although bound by external levees and inner levees, were able to migrate laterally up to SH –Q3 > 1000 m (Fig. 11B). There is also evidence that the Hikurangi Channel with an unconfined character and coeval channel-levee build up shows clear lateral growth of its channel elements (McArthur and Tek, 2021; Tek et al., 2021). The basin scale complexes within the Bengal Fan (Kolla et al., 2012), despite constraint by regional slope valleys, can freely migrate laterally and vertically to reach SH –Q3 > 4000 m (Fig. 11B). As an exception, the available data of the Dalia M9 channels presents lower SH records than the Fulani channel. It is conceivable that this quantitative difference is caused by the available cross-sectional data (n=5), in which all examples where from confined channels intensively entrenched into stacked internal levees (Abreu et al., 2003). Therefore, the migrations of the LAPs were dramatically constrained. Except the Dalia M9 Channels, our comparison of the Fulani Channel with the unstructured complexes indicate a difference of +1.3 km SH mean values (Fig. 11B). Therefore, the intrinsic controls via the dominance of bank collapses have a role to limit channel lateral migrations despite the development around active growing structures.

Comparison of structurally and non-structurally influenced submarine channels (Fig. 11B), demonstrates that channel kinematics are mainly regulated by configuration of the formative channels' erosional base and levee build-up. Moreover, this study provides new insights into the potential limitations of channel migration which can counter the structural influence by the dominance of wall failure deposits.

7. CONCLUSIONS

Considering the role of submarine channels in shaping the stratigraphic archives of deep-sea fans, we were determined to examine how they evolved by interaction with bank failure mass-transport deposits. We addressed the interaction of two channel complexes belonging to the Upper Miocene-Pleistocene Fulani Channel, which developed across actively growing folds in the Outer fold and thrust belt domain of the Niger Delta. Our data allow us to quantitatively analyze the cross-sectional parameters (width, lateral shift, thickness, aspect ratio, and depositional ratios), and channel planform (sinuosity, meander amplitude), to explore their relationships with MTD ratios and the underlying structural gradients. The main results are as follows:

(1) The relationships between sinuosity, meander amplitude, and cross-sectional parameters depend on the way in which wall collapses removed and accumulated material in channels. Where MTD ratios are less than 30%, they promote a coherent relationship of these parameters. However, where they exceed 30%, the parameters tend to exhibit anomalous relationships.

(2) Channel planform architectures record a depositional response to growth of structures through meander amplitude over scales of >18 km along the channel. However, sinuosity is only sensitive to bank failure MTDs at a smaller scale, forcing channel swings over sections ranging from 1 to 3.5 km (e.g., segments U1, 2*, 4" and 7*).

(3) Under conditions of simultaneous confinement by of channel bank failure MTDs and structural forcing – i.e., with structural gradient (SG) greater than 30% – the compensation relationships lead to vertical channel stacking at a high stratigraphic position (i.e., channel C2). However, when bank failure MTDs exceed critical levels (>40% MTD ratio), resulting in rapid channel fill, this condition promoted subsequent flow relaxation, characterized by lateral channel stacking at an elevated stratigraphic position in the channel system. Presumably, this lateral stacking is due to the equilibrium gradient that has been distributed by aggradation of the channel complex base and the elemental channels have less rood to agrade.

(4) Channel thickness is insensitive to wall-collapses except at critical confinements produced by MTDs combined with structural deformation, but are generally not representative for the kinematics of the Fulani Channel.

(5) The limit of channel migration is fixed by bank failures at any given stratigraphic position, and regardless of the structural influence, a threshold of 1.7 km width is recorded in the Fulani Channel. This caused the coeval structural growth to force only the lateral offsets of channel elements but not constrain the lateral mobility of channel complexes.

(6) Channel lateral shift (SH) is a key indicator of lateral migration, and in the case of the Fulani Channel, it correlates with the widths of channel complexes and the lateral mobility of their constituent elements. SH is particularly sensitive to the collapses of channel walls in conjunction with levee confinements. The prevalence of bank failure MTDs in the Fulani Channel induces limited SH ranges when compared to other structurally deflected channels (SH mean: –1.1 km) and the majority of unstructured channels (SH mean: -0.5 km).

(7) Therefore, by contextualizing our data with a global quantitative data sets of submarine channels, we show for the first time that channel bank failure MTDs can counteract the structural influence on submarine channel kinematics, and change the properties of lateral migrations. This insight can be used to help understand the sedimentary archives of other deep-marine sedimentary systems and the dispersal of sediments and organic carbon in channels across continental margins.

ACKNOWLEDGEMENENTS

We thank CNOOC (China National Oil Offshore Corporation) for providing the data set and for the permission to show and publish the three-dimensional seismic survey. This work presented in this paper is financially supported by National Natural Science Foundation of China-NSFC (no. 42072183, and 41872142). D. Gamboa thanks the financial support to CESAM by the Portuguese Fundação para a Ciência e a Tecnologia (FCT) I.P./MCTES through national funds (PIDDAC) UIDP/50017/2020, UIDB/50017/2020, and LA/P/0094/2020. We thank Editor Kerry Gallagher and reviewers Rufus Brunt and Bryan Cronin for their expert advice.

REFERENCES

Abreu, V., Sullivan, M., Pirmez, C., Mohrig, D., 2003. Lateral accretion packages (LAPs): an important reservoir element in deep water sinuous channels. Marine and Petroleum Geology. 20: 631-648.

Babonneau, N., Savoye, B., Cremer, M., Klein, B., 2002. Morphology and architecture of the present canyon and channel system of the Zaire deep-sea fan. Mar. Petrol. Geol. 20, 445–467. https://doi.org/10.1016/S0264-8172(02)00009-0.

Bouchakour, M., Zhao, X., Ge. J., Miclăus, C., Yang, B., 2022. Evolution of submarine channel morphology in intra-slope mini-basins: 3D-seismic interpretation from offshore Niger Delta. Marine and Petroleum Geology 146: 105912. https://doi.org/10.1016/j.marpetgeo.2022.105912

Bouchakour, M., Zhao, X., Miclăus, C., Liu, F., Gamboa, D., Yang, B., 2024. Compartmentalization of submarine channel splays controlled by growth faults and mud diapir. Marine and Petroleum Geology. http://dx.doi.org/10.2139/ssrn.4756543.

Briggs, S.E., Davies, R.J., Cartwright, J.A., Morgan, R., 2006. Multiple detachment levels and their control on fold styles in the compressional domain of the deepwater west Niger Delta. Basin Res. 18, 435-450.

Clark, I.R , and J.A Cartwright., 2012. Interactions between coeval sedimentation and deformation from the Niger Delta deep-water fold belt. SEPM Spec. Publ. No. 99: 243-267.

Clark, I.R, and J.A Cartwright., 2009. Interactions between submarine channel systems and deformation in deep-water fold belts: examples from the Levant Basin, Eastern Mediterranean sea. Marine and Petroleum Geology. 26: 1465-1482.

Clark, IR, and J.A Cartwright., 2011. Key controls on submarine channel development in structurally active settings. Marine and Petroleum Geology. 28: 1333-1349.

Clark, J.D., and Pickering, K.T., 1996, Submarine Channels: Processes and Architecture: London, Vallis Press, 231 p.

Corella, J.P., Loizeau, J.L., Kremer, K., Hilbe, M., Gerard, J., Le Dantec, N., Stark, N., Gonzalez-Quiano, M., and Giradclos, S., 2016, The role of mass-transport deposits and turbidites in shaping modern lacustrine deepwater channels: Marine and Petroleum Geology, v. 77, p. 515–525.

Corredor, F., Shaw, J.H., Bilotti, F., 2005. Structural styles in the deep-water fold and thrust belts of the Niger Delta. AAPG Bull. 89 (6): 753-780.

Covault, J.A., Sylvester, Z., Ceyhan, C., Dunlap, D., 2021. Giant meandering channel evolution, Campos deep-water salt basin, Brazil. Geosphere. 17 (6): 1896–1889.

Covault, J.A., Sylvester, Z. and Dunlap, D.B., 2024. Submarine-channel meandering reset by landslide filling, Taranaki Basin, New Zealand. *The Depositional Record*.

Covault, J.A., Sylvester, Z., Hudec, M.R., Ceyhan, C., and Dunlap, D., 2019. Submarine channels 'swept' downstream after bend cutoff in salt basins. The Depositional Record, 6: 259-272.

Cronin, B.T., the Jubilee Team, Tullow Ghana Limited., 2022. Giant pockmark-initiated deep-water slope channel complexes. *AAPG Bulletin*, V. 106, No. 04. Pp. 829-868. https://doi.org/10.1306/11042118179

Cronin, B.T., Kenyon, N.H., Woodside, J., den Bezemer, T., van der Wal, A., Millington, J., Ivanov, M.K., Limonov, A., 1995. The Almeria Canyon: a meandering channel system on an active margin, Alboran Sea, Western Mediterranean. In: Pickering, K.T., Hiscott, R.N., Kenyon, N.H., Ricci Lucchi, F., Smith, R.D.A. (eds) Atlas of Deep Water Environments. Springer, Dordrecht. https://doi.org/10.1007/978-94-011-1234-5_15

Cullis, S., Colombera, L., Patacci, M., McCaffrey, W.D., 2018. Hierarchical classifications of the sedimentary architecture of deep-marine depositional systems. Earth Sci. Rev. 179: 38–71.

Damuth, J.E., 1994. Neogene gravity tectonics and depositional processes on the deep Niger Delta continental margin. Marine and Petroleum Geology. 11: 320-346.

Deptuck, M., Steffens, G.S., Barton, M., Pirmez, C., 2003. Architecture and evolution of upper fan channel-belts on the Niger Delta slope and in the Arabian sea. Mar. Petrol. Geol: 649–676. https://doi.org/10.1016/j.marpetgeo.2003.01.004.

Deptuck, M.E, Z Sylvester, C Pirmez, and C., O'Byrne., 2007. Migration–aggradation history and 3-D seismic geomorphology of submarine channels in the Pleistocene Benin major Canyon, western Niger Delta slope. Marine and Petroleum Geology. 24: 406-433.

Dimitrov, L.I., 2002. Mud volcanoes—the most important pathway for degassing deeply buried sediments. Earth-Science Reviews, 59. pp. 49-76

Doust, H., Omatsola, E., 1990. Niger delta. In: Edwards, J.D., Santogrossi, P.A. (Eds.), Divergent/passive Margin Basins. American Association of Petroleum Geologists: 201-238.

Evamy, B., J. Haremboure, P. Kamerling, W. Knaap, F. Molloy, and P. Rowlands, 1978, Hydrocarbon habitat of Tertiary Niger Delta: AAPG Bulletin, v. 62, no. 1, p. 1–39, doi:10.1306/C1EA47ED-16C9-11D7-8645000102C1865D.

Gamberi, F., Rovere, M., 2011. Architecture of a modern transient slope fan (Villafranca fan, Gioia basineSoutheastern Tyrrhenian Sea). Sediment. Geol. 236, 211e225. http://dx.doi.org/10.1016/j.sedgeo.2011.01.007.

Gee, M.J.R., Gawthorpe, R.L., 2006. Submarine channels controlled by salt tectonics: examples from 3D seismic data offshore Angola. Marine and Petroleum Geology. 23: 443-458.

Gee, M.J.R., Gawthorpe, R.L., Bakke, K., Friedmann, S.J., 2007. Seismic geomorphology and evolution of submarine channels from the Angolan continental margin. J. Sediment. Res. 77: 433–446.

Gong, C., Steel, R. J., Qi. K., Wang. Y., 2021. Deep-water channel morphologies, architectures, and population densities in relation to stacking trajectories and climate states: Geological Society of America Bulletin, v. 133, no. 1–2: 287–306, doi:10.1130/B35431.1.

Goodwin, Prior, 1989. Geometry and depositional sequences of the Mississippi Canyon, Gulf of Mexico. Journal of Sedimentary Petrology 59, 318-329.

Hansen, L, Callow, R.H.T, Kane, I, F Gamberi, M Rovere, B.T Cronin, and Kneller, B., 2015. Genesis and character of thin-bedded turbidites associated with submarine channels. Marine and Petroleum Geology. 67: 852-879.

Hansen, L., L'Heureux, J.S., Sauvin, G., Polom, G., Lecomte, I., Vaneste, M., Longva, O., and Krawczyk, C., 2013. The effect of mass-wasting on the stratigraphic architecture of a fjord-valley fill: correlation of onshore, shear wave seismics and marine seismic data at Trondheim, Norway: Sedimentary Geology, v. 289, p. 1–18.

Hodgson, D.M., Di Celma, C. N., Brunt, R.L., Flint, S.S., 2011. Submarine slope degradation and aggradation and the stratigraphic evolution of channel–levee systems: Journal of the Geological Society, v. 168, pp. 625–628. doi: 10.1144/0016-76492010-177.

Howlett, D.M., Gawthorpe, R.L., Ge, Z., Rotevatn, A., Jackson, C., 2020. Turbidites, topography and tectonics: Evolution of submarine. Basin Reaserch. doi: https://doi.org/10.1111/bre.12506.

Iglesias J., Ercilla G., García-Gil S., Judd AG., 2010. Pockforms: an evaluation of pockmark-like seabed features on the Landes Plateau, Bay of Biscay. Geo Mar Lett 30(3/4):207–219. doi:10.1007/s00367-009-0182-2

Janocko, M., Nemec, W., Henriksen, S., & Warchoł, M., 2013. The diversity of deep-water sinuous channel belts and slope valley-fill complexes. Mar. Petrol. Geol, 41: 7–34.

Jobe, Z.R., Howes, N. C., Straub, K.M., Cai, D., Deng, H., Laugier, F.J., Pettinga, L.A., Shumaker, L.E., 2020. Comparing Aggradation, Supperelevation, and Avulsion Frequency of Submarine and Fluvial Channels. Front. Earth Sci: 8-53. https://doi.org/10.3389/feart.2020.00053.

Jobe, Z. R., Sylvester, Z., Parker, A. O., Howes, N. C., Slowey, N., Pirmez, C., 2015. Rapid adjustment of submarine channel architecture to changes in sediment supply. Journal of Sedimentary Research, 85(6): 729–753, doi:10.2110 /jsr.2015.30.

Jolly, B.A., Lonergan, L., Whittaker, A.C., 2016. Growth history of fault-related folds and interaction with seabed channels in the toe-thrust region of the deep-water Niger delta. Marine and Petroleum Geology. 70: 58-76.

Kane, I.A., and Clare, M.A., 2019, Dispersion, accumulation, and the ultimate fate of microplastics in deep-marine environments: A review and future directions: Frontiers in Earth Sciences, v. 7, 80, https://doi.org/10.3389/feart.2019.00080.

Kertznus, V., 2009, Stratigraphic Development of Delta-Fed Slope Systems: Offshore Ebro and Nile Deltas [Ph.D. thesis]: University of Aberdeen, 298 p.

Kilhams, B., McArthur, A., Huuse, M., Ita, E. and Hartley, A., 2011. Enigmatic large-scale furrows of Miocene to Pliocene age from the central North Sea: current-scoured pockmarks?. Geo-Marine Letters, 31, pp.437-449.

Klaucke, I., Hesse, R., Ryan, W.B.F., 1998. Seismic stratigraphy of the Northwest Atlantic Mid-Ocean Channel: growth pattern of a mid-ocean channel-levee complex. Mar. Pet. Geol. 15 (6), 575e585. http://dx.doi.org/10.1016/S02648172(98)00044-0.

Kneller, B., Dykstra, M., Fairweather, L., Milana, J.P., 2016. Mass-transport and slope accommodation: implications for turbidite sandstone reservoirs. AAPG Bull. 100: 213–235.

Kolla, V., Bandyopadhyay, A., Gupta, P., Mukherjee, B., and Ramana, D.V., 2012, Morphology and internal structure of a recent upper Bengal fan-valley complex, in Prather, B.E., Deptuck, M.E., Mohrig, D., Van Hoorn, B., and Wynn, R.B., eds., Application of the Principles of Seismic Geomorphology to Continental Slope and Base-of-Slope Systems: Case Studies from Seafloor and Near-Seafloor Analogues: SEPM (Society for Sedimentary Geology) Special Publication 99, p. 347–369, https:// doi .org /10 .2110 /pec .12 .99 .0347.

Kremer, C.H., McHargue, T., Scheucher, L., Graham, S.A., 2018. Transversely-coursed mass-transport deposits and stratigraphic evolution of a foreland submarine channel system: Deep-water tertiary strata of the Austrian Molasse Basin. Mar. Pet. Geol. 92: 1-19.

Lamb, M.P., Parsons, J.D., Mullenbach, B.L., Finlayson, D.P., Orange, D.L., Nittrouer, C.A., 2008. Evidence for superelevation, channel incision, and formation of cyclic steps by turbidity currents in Eel Canyon, California. Geol. Soc. Am. Bull. 120, 463e475. http://dx.doi.org/10.1130/B26184.1.

Li, S., Gong, C., 2016. Flow dynamics and sedimentation of lateral accretion packages in sinuous deep-water channels: A 3D seismic case study from the northwestern South China Sea margin. Journal of Asian Earth Sciences. 124, 233-246. http://dx.doi.org/10.1016/j.jseaes.2016.05.008

Liu, L., Zhang, T., Zhao, X., Wu, S., Hu, J., Wang, X., Zhang, Y., 2013. Sedimentary architecture models of deep-water turbidite channel systems in the Niger Delta continental slope, West Africa. Petrol. Sci. 10, 139–148.

Maloney, D., Davies, R., Imber, J., Higgins, S., & King, S. (2010). New insights into deformation mechanisms in the gravitationally driven Niger Delta deep-water fold and thrust belt. AAPG Bulletin, 94, 1401–1424.

Masalimova, L., Lowe, D.R., McHargue, T., and Derksen, R., 2015, Interplay between an axial channel belt, slope gullies and overbank deposition in the Puchkirchen Formation in the Molasse Basin, Austria: Sedimentology, v. 62, p. 1717–1748.

Mayall, M., E. Jones, Casey, M., 2006. Turbidite channel reservoirs—Key elements in facies prediction and effective development. Marine and Petroleum Geology 23: 821–841. doi:10.1016/j.marpetgeo.2006.08.001.

Mayall, M., Lonergan, L., Bowman, A., James, S., Mills, K., Primmer, T., Pope, D., Rogers, L., and Skeene, R., 2010. The response of turbidite slope channels to growth-induced seabed topography. AAPG Bulletin. 94: 1011-1030

McArthur, A.D., Kneller, B.C., Souza, P.A., Kuchle, J., 2016a. Characterization of deepmarine channel-levee complex architecture with palynofacies: an outcrop example from the Rosario Formation, Baja California, Mexico. Mar. Petroleum Geol. 73, 157e173. http://dx.doi.org/10.1016/j.marpetgeo.2016.02.030.

McArthur, A.D. and Tek, D.E., 2021. Controls on the origin and evolution of deep-ocean trench-axial channels. Geology, 49(8), pp.883-888.

McArthur, A.D., Tek, D., Poyatos-Moré, M., Colombera, L., McCaffrey, W., 2024. Deep-ocean channel-wall collapse order of magnitude larger than any other documented. Communications earth & environment, 5:143. https://doi.org/10.1038/s43247-024-01311-z

McHargue, T.R., Pyrcz, M. J., Sullivan, M. D., Clark, J. D., Fildani, A., Romans, B. W., Covault, J. A., Levy, M., Posamentier, H. W., & Drinkwater, N. J., 2011. Architecture of turbidite channel systems on the continental slope: Patterns and predictions. Mar. Petrol. Geol. 28 (3): 728–743.

Mitchell, W.H., Whittaker, A., Mayall, M., Lonergan, L., Pizzi, M., 2021a. Quantifying structural controls on submarine channel architecture and kinematics. GSA Bulletin. 134 (3-4), 928-940. doi: https://doi.org/10.1130/B36001.1

Mitchell, W.H., Whittaker, C., Mayall, M., Lonergan, L., 2021b. New models for submarine channel deposits on structurally complex slopes: Examples from the Niger delta system. Marine and Petroleum Geology 129: 105040. doi: https://doi.org/10.1016/j.marpetgeo.2021.105040.

Moscardelli, L., Wood, L., Mann, P., 2006. Mass-transport complexes and associated processes in the offshore area of Trinidad and Venezuela. AAPG Bull. 90: 1059–1088.

Mulder, T., E Ducassou, H Gillet, Hanquiez, V., Tournadour, E., Combes, J., P Elberli, G., Kindler, P., Gonthier, E., Gonesa, G., 2012. Canyon morphology on a modern carbonate slope of the Bahamas: evidence of regional tectonic tilting. Geology 40, 771–774.

Nakajima, T., Peakall, J., McCaffrey, W. D., Paton, D. A., & Thompson, P. J. P., 2009. Outer-bank bars: A new intra-channel architectural element within sinuous submarine slope channels. Journal of Sedimentary Research, 79: 872–886.

Nakajima, T., Satoh, M., Okamura, Y., 1998. Channel-levee complexes, terminal deepsea fan and sediment wave fields associated with the Toyama Deep-Sea channel system in the Japan Sea. Mar. Geol. 147, 25e41. http://dx.doi.org/10.1016/S00253227(97)00137-0.

Navarre, J.-C., Claude, D., Librelle, F., Safa, P., Villon, G., Keskes, N., 2002. Deepwater turbidite system analysis, West Africa: sedimentary model and implications for reservoir model construction. Lead. Edge 21, 1132–1139.

Nelson, C.H., Escutia, C., Goldfinger, C., Karabanov, E., Gutierrez-pastor, J., and Debatis, M.., 2009, External controls on modern clastic turbidite systems: three case studies, in Kneller, B.C., Martinsen, O.J., and McCaffrey, W.D., eds., External Controls on Deep-Water Depositional Systems: SEPM, Special Publication 96, p. 57–76.

Olayiwola, M. A., Bamford, M. K., & Durugbo, E. U. (2017). Graphic correlation: A powerful tool for biostratigraphic correlation of petroleum exploration and production in the Cenozoic deep offshore Niger Delta, Nigeria. Journal of African Earth Sciences, 131, 156–165.

Oluboyo, A.P., Gawthorpe, R.L., Bakke, K., Hadler-Jacobsen, F., 2014. Salt tectonic controls on deep-water turbidite depositional systems: Miocene, southwestern Lower Congo Basin, offshore Angola. Basin Research. 26. 597-620.

Ortiz-Karpf, A., Hodgson, D.M., McCaffrey, W.D., 2015. The role of mass-transport complexes in controlling channel avulsion and the subsequent sediment dispersal patterns on an active margin: the Magdalena Fan, offshore Colombia. Marine and Petroleum Geology. 64, 58–75.

Payton, C.E., 1977. Seismic Stratigraphy - Application to Hydrocarbon Exploration. AAPG Memoir 26, Tulsa, OK.

Peakall, J., McCaffrey, B., Kneller, B., 2000. A process model for the evolution, morphology, and architecture of submarine channels. J. Sediment. Res. 70, 434–448. Picot, M., et al., 2019. Monsoon control on channel avulsions in the late quaternary Congo fan. Quat. Sci. Rev. 204, 149–171.

Pickering, K.T., Corregidor, J., 2005. Mass-transport complexes (mtcs) and tectonic control on basin- £oor submarine fans, Middle Eocene, South Spanish Pyrenees. J. Sediment. Res. (75), 761.

Piper, D.J.W., and Normark, W.R., 2001, Sandy fans—From Amazon to Hueneme and beyond: American Association of Petroleum Geologists Bulletin, v. 85, p. 1407–1438, https:// doi .org /10 .1306 /8626CACD -173B -11D7 -8645000102C1865D.

Pizzi, M., Lonergan, L., Whittaker, A.C., Mayall, M., 2020. Growth of a thrust fault array in space and time: an example from the deep-water Niger delta. J. Struct. Geol. https://doi.org/10.1016/j.jsg.2020.104088.

Posamentier, H.W., 2003, Depositional elements associated with a basin floor channel-levee system: case study from the Gulf of Mexico: Marine and Petroleum Geology, v. 20, p. 677–690, https://doi .org/10.1016/ j.marpetgeo.2003.01.002.

Posamentier, H.W., Davies, R.J., Cartwright, J.A., Wood, L., 2007. Seismic geomorphology-an overview. In: Davies, R.J., Posamentier, H.W., Wood, L.J., Cartwright, J.A. (Eds.), Seismic Geomorphology: Applications to Hydrocarbon Exploration and Production 277. Geological Society, London, Special Publications:1–14.

Posamentier, H.W., Kolla, V., 2003. Seismic geomorphology and stratigraphy of depositional elements in deep-water settings. Journal of Sedimentary Research. 73: 367-388.

Posamentier, H., Martinsen, O., 2011. The character and genesis of submarinemass-transport deposits: insights from outcrop and 3D seismic data. In: Verwer, K., Playton, T., Harris, P. (Eds.), Mass-transport Deposits in Deepwater Settings, vol. 96. SEPM Special Publication: 7–38.

Prather, B. E., 2003. Controls on reservoir distribution, architecture and stratigraphic trapping in slope settings. Marine and Petroleum Geology. v. 20, no. 6–8, p. 529– 545. doi:10.1016/j.marpetgeo.2003.03.009.

Prather, B.E., Booth, J.R., Steffens, G.S., Craig, P.A., 1998. Classification, lithologic calibration and stratigraphic succession of seismic facies from intraslope basins, deep water Gulf of Mexico, U.S.A. AAPG Bull. 82: 701 – 728.

Pringle, J.K., Brunt, R.L., Hodgson, D.M., Flint, S.S., 2010. Capturing stratigraphic and sedimentological complexity from submarine channel complex outcrops to digital 3D models, Karoo Basin, South Africa. Petroleum Geoscience, V. 16, pp. 307-330. DOI 10.1144/1354-079309-028.

Qin, Y., Alves, T.M., Constantine, J., Gamboa, D., 2016. Quantitative seismic geomorphology of a submarine channel system in SE Brazil (Espírito Santo Basin): scale comparison with other submarine channel systems. Mar. Petrol. Geol. 78: 455–473.

Qin, Y., Alves, T.M., Constantine, J., Gamboa, D., Wu, S., 2019. Effect of channel tributaries on the evolution of submarine channel confluences (Espírito Santo Basin, SE Brazil). GSA Bulletin. 134 (1-2), 263–272. https://doi.org/10.1130/B35082.1.

Rouby, D., Nalpas, T., Jermannaud, P., Robin, C., Guillocheau, F., Raillard, S., 2011. Gravity driven deformation controlled by the migration of the delta front: the Plio-Pleistocene of the eastern Niger Delta. Tectonophysics. 513: 54-67.

Rowan, M.G., Peel, F.J., Vendeville, B.C., 2004. Gravity-driven fold belts on passive margins. In: McClay, K.R. (Ed.), Thrust Tectonics and Hydrocarbon Systems. AAPG Memoir. 82: 157-182.

Saller, A., Njoman, I., Dharmasamadhi, W., 2012. Controls on the development of valleys, canyons, and unconfined channelelevee complexes on the Pleistocene Slope of East Kalimantan, Indonesia. Mar. Pet. Geol. 29: 15-34. doi:10.1016/j.marpetgeo.2011.09.002.

Sawyer, D.E., Flemings, P.B., Shipp, R.C., Winker, C.D., 2007. Seismic geomorphology, lithology, and evolution of the late Pleistocene Mars-Ursa turbidite region, Mississippi Canyon area, northern Gulf of Mexico. AAPG Bull. 91, 215e234. http://dx.doi.org/10.1306/08290605190.

Sawyer, D.E., Flemings, P.B., Nikolinakou, M., 2013. Continuous deep-seated slope failure recycles sediments and limits levee height in submarine channels. Geology 42, 15e18. http://dx.doi.org/10.1130/G34870.1.

Short, K.C., Stäuble, A.J., 1967. Outline of geology of Niger delta. AAPG Bull 51: 761-779.

Smith, D.P.,Ruiz, G., Kvitek, R., Iampietro, P.J., 2005. Semiannual patterns of erosion and deposition in upper Monterey Canyon from serial multibeam bathymetry. GSA Bulletin. v. 117; no. 9/10; p. 1123–1133; doi: 10.1130/B25510.1.

Sprague, A.R.G., Garfield, T.R., Goulding, F.J., Beaubouef, R.T., Sullivan, M.D., Rossen, C., Cmapion, K.M., Sickafoose, D.K., Abreu, V., Schellpeper, M.E., Jensen, G. N., Jennette, D.C., Pirmez, C., Dixon, B.T., Ying, D., Ardill, J., Mohrig, D.C., Porter, M.L., Farrell, M.E., Mellere, D., 2005. Integrated Slope Channel Depositional Models: the Key to Successful Prediction of Reservoir Presence and Quality in Offshore West Africa.

Spina, V., Mazzoli, S., 2023. Shale 3D Flow and Interaction With Basement Faults in the Niger Delta Deep Water Fold and Thrust Belt. Tectonics. 42 (12): e2023TC007957. https://doi.org/10.1029/2023TC007957.

Sylvester, Z., Pirmez, C., & Cantelli, A., 2011. A model of submarine channel-levee evolution based on channel trajectories; implications for stratigraphic architecture. Mar. Pet. Geol. 28: 716–727. doi:10.1016/j.marpetgeo.2010.05.012.

Tek, D.E., McArthur, A.D., Poyatos-Moré, M., Colombera, L., Patacci, M., Craven, B. and McCaffrey, W.D., 2021. Relating seafloor geomorphology to subsurface architecture: how mass-transport deposits and knickpoint-zones build the stratigraphy of the deepwater Hikurangi Channel. Sedimentology, 68(7), pp.3141-3190.

Vail, P.R., Mitchum, R.M., Thompson, S., 1977a. Seismic stratigraphy and global changes of sea level, part 3: relative changes of sea level from coastal onlap. In: Payton, C.E. (Ed.), Seismic Stratigraphy - Applications to Hydrocarbon Exploration, AAPG Memoir, vol. 26, pp. 63–81.

Ward, I.P.N., Alves, M.T., Blenkinsop, G.T., 2018. Submarine sediment routing over a blocky mass-transport deposit in the Espirito Santo Basin, SE Brazil. Basin Res. 30: 816–834.

Wynn, R.B., Cronin, B.T. and Peakall, J., 2007. Sinuous deep-water channels: Genesis, geometry and architecture. Marine and Petroleum Geology 14 (6): 341-387.

Zhang, J., Wu, S., Hu, G., Fan, T., Yu, B., Lin, P., Jiang, S., 2018. Sea-level control on the submarine fan architecture in a deepwater sequence of the Niger Delta Basin. Mar. Petrol. Geol. 94: 179–197.

Zhao, X., Qi, K., Patacci, M., Chengpeng, T and Xie, T., 2019. Submarine channel network evolution above an extensive mass-transport complex: A 3D seismic case study from the Niger delta continental slope. Marine and Petroleum Geology (104): 231-248.

Zhao, X.M., Qi, K., Liu, L., Gong, C.L., McCaffrey, W.D., 2018. Development of a partially-avulsed submarine channel on the Niger Delta continental slope: architecture and controlling factors. Marine and Petroleum Geology. 95: 30-49.

LIST OF FIGURES

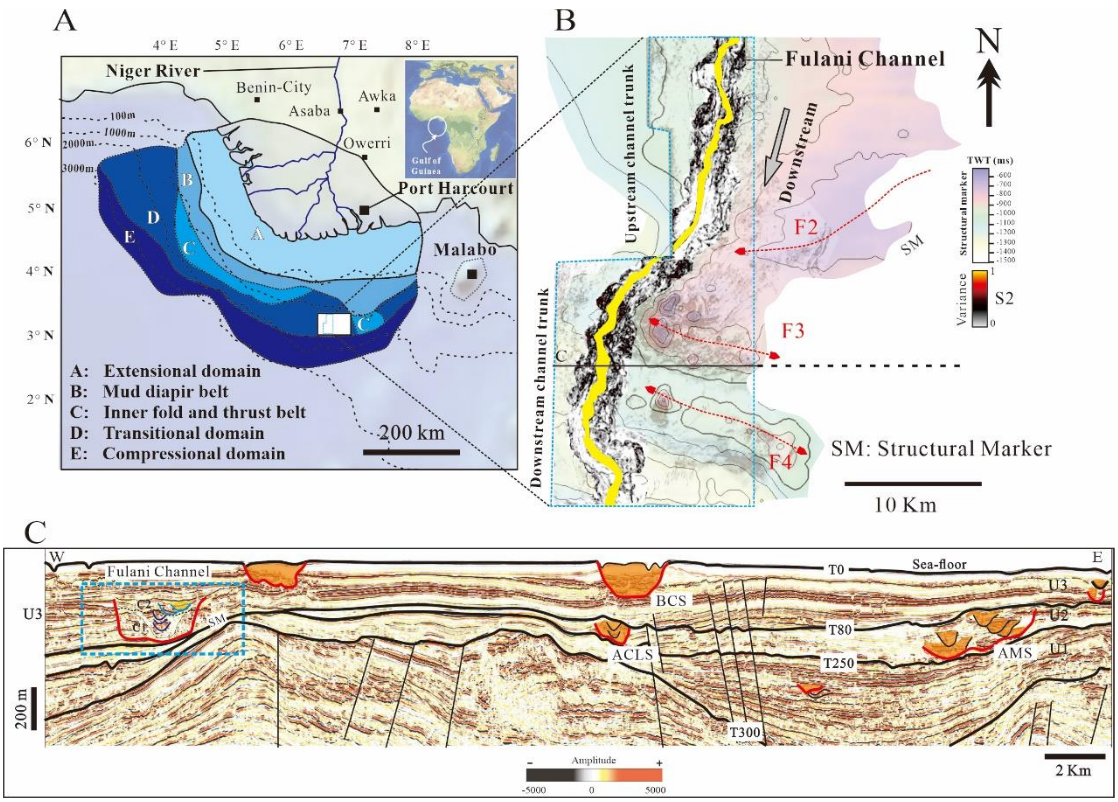

Figure 1. (A) Map showing the location of the study area (white box) in the eastern Niger Delta. The major structural domains are also shown (modified from Corredor et al., 2005 and Jolly et al., 2016). (B) Variance attributes map showing the location of the Fulani Channel (youngest channel element in yellow), with time structure map overlay the structural marker (SM). Note that the variance attribute map is extracted from the key horizon of the channel C2 (blue line below the C2's final channel in Fig. 5B-C; see also Supplementary Material Fig. 4C). (C) Seismic cross-section perpendicular to dip direction of channels, showing the stratigraphic framework and location of the Fulani Channel together with other systems of the study area: Amaku Channel Levee System (ACLS), Amaku Major System (AMS) (Bouchakour et al., 2022 and 2023), and Bukuma Channel System (BCS) (Zhao et al., 2019).

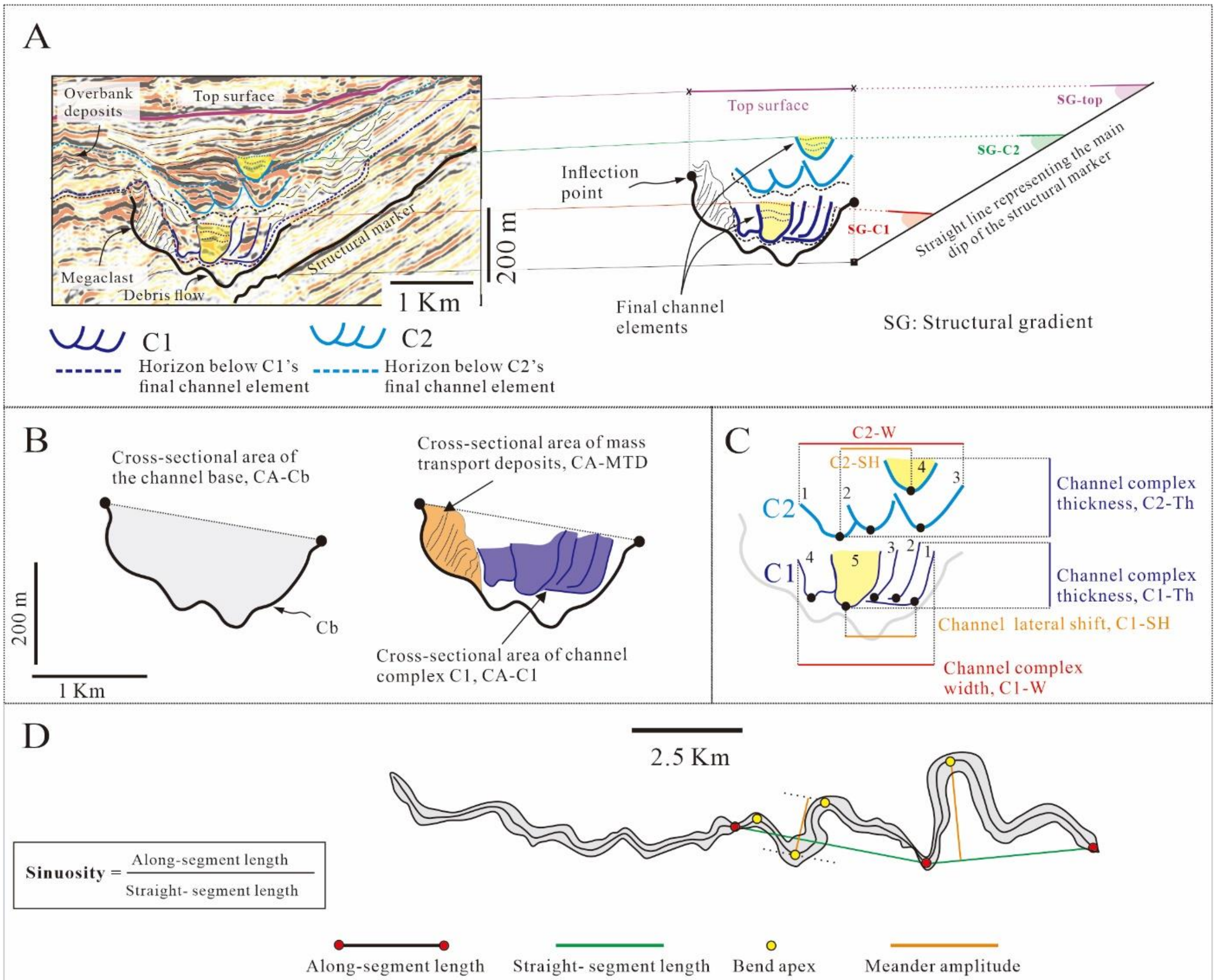

Figure 2. (A) Interpreted cross-section (section 3) of the Fulani Channel. The channel complexes C1 and C2 are highlighted and their final channel elements colored in yellow. At top right, is a schematic illustration of structural gradient measurements in relation to the youngest elements of channel complexes C1 and C2, and the top surface shown in purple. (B) Schematic illustration of cross-sectional areas interpretation: CA-Cb (Cross-sectional Area of Channel base), CA-MTD (Cross-sectional Area of MTD), and CA-C1 (Cross-sectional Area of C1). (C) Schematic illustration of channel complex interpretation showing width, thickness, and lateral shift adapted from Bouchakour et al. (2023). (D) Illustration of the final channel element of C1, showing the planform measurements; sinuosity and meander amplitudes.

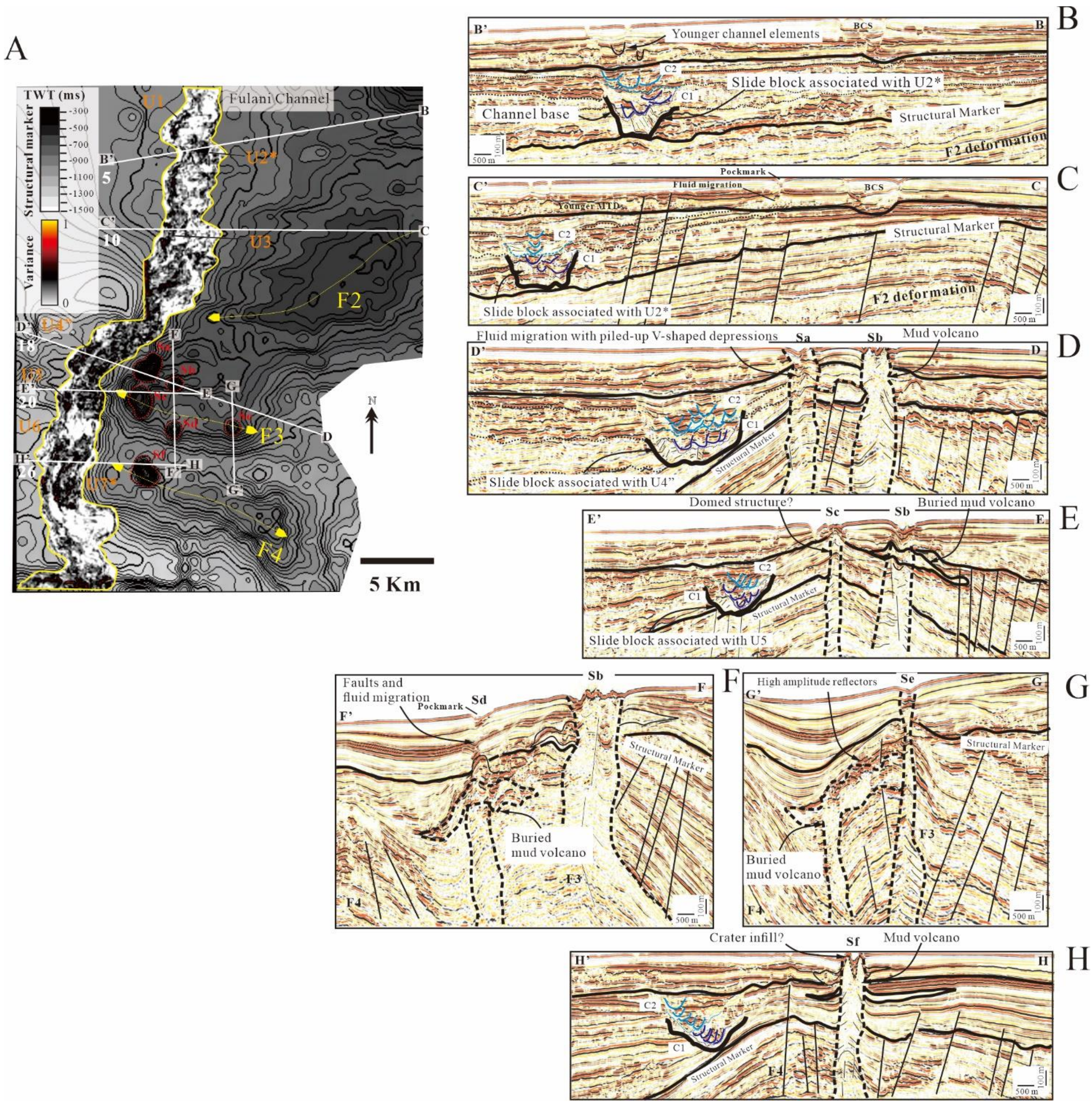

Figure 3. (A) Time structure map extracted from the structural marker showing the geological structures associated with the Fulani Channel, including folds (F2, F3, and F4) and structures (Sa-Sf). Variance attribute map of the erosional base is also shown (See also Supplementary Material Fig. 4). (B-H) Cross-sections showing details of the folds and their structures, including mud volcanoes, fluid migrations, domes, and pockmark depressions. Note that Figs. B and C are extracted from the upstream channel trunk, and Figs. C-H from the downstream channel trunk.

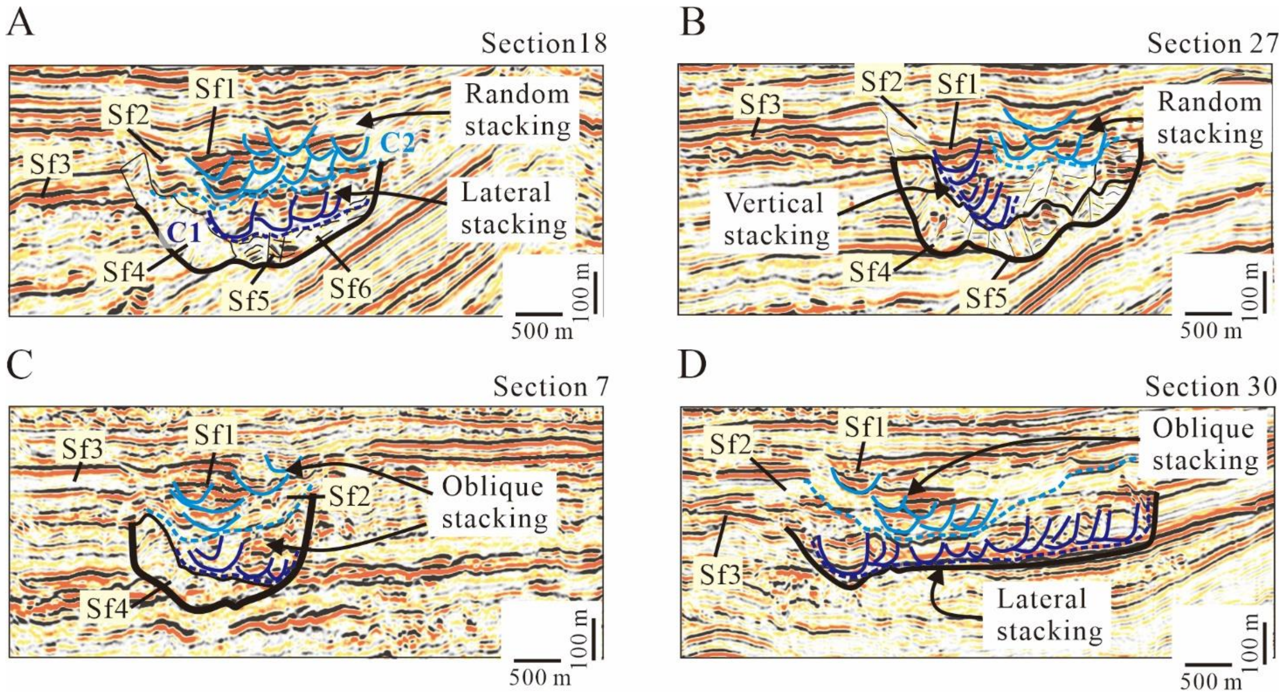

Figure 4. Types of architectures observed in channel complexes (C1 and C2). Cross-sections showing examples of random stacking elements (A), vertical stacking elements (B), oblique stacking elements (C), and lateral stacking elements (D). Seismic facies Sf1, Sf2, Sf3, Sf4, Sf5, and Sf6 are also shown.

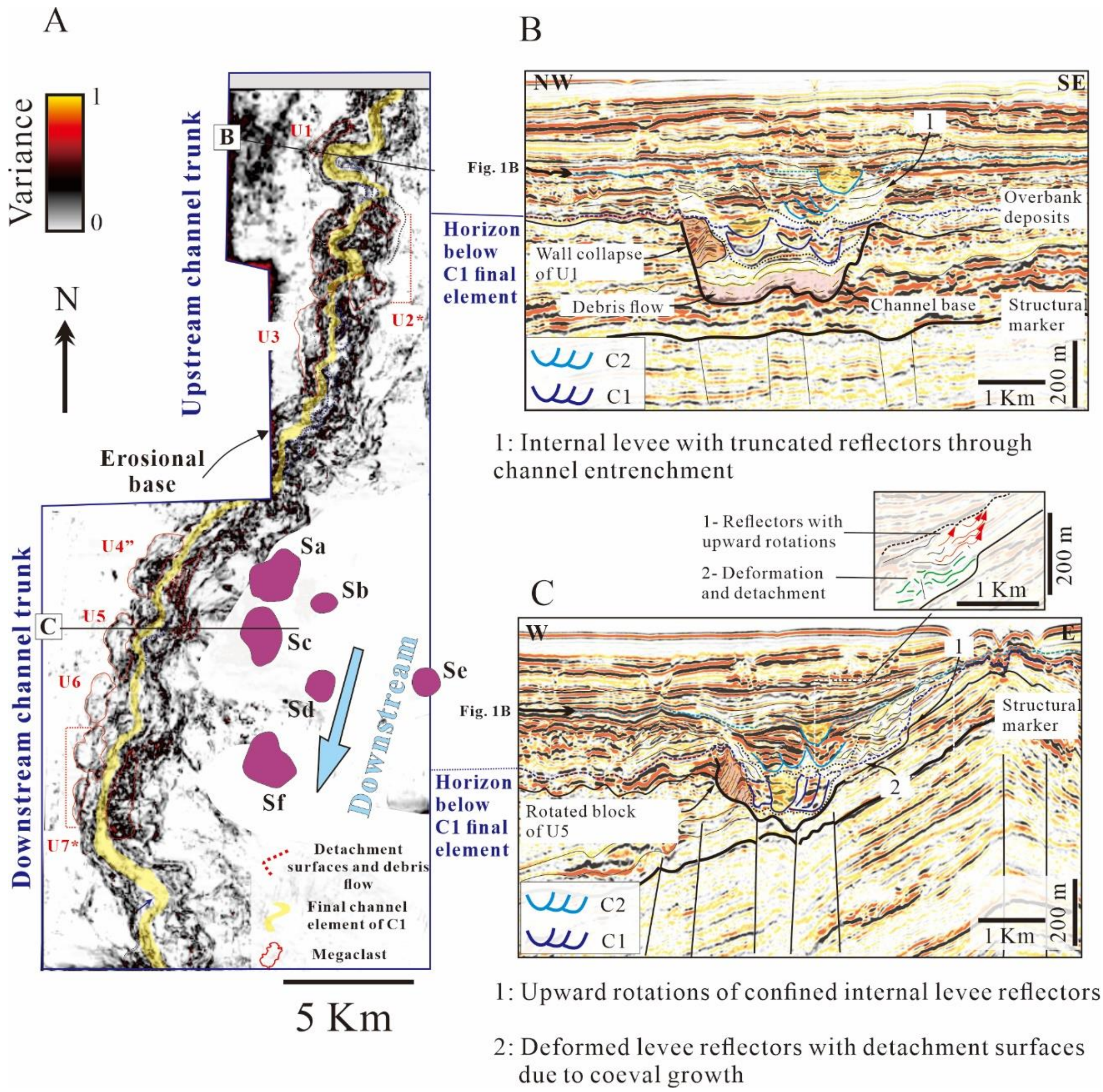

Figure 5. (A) Variance attribute map extracted at the final channel of C1 (yellow color pathway). The channel base bounding surface is indicated by dark color amplitudes. The mass transport deposits (MTDs) units and structures are indicated. See the uninterpreted map in Supplementary Material Fig. 4. MTDs distributed on both channel margins are shown with asterisk (*), and the one associated with slide blocks and debris flows in the channel axis by double quotation (”). (B) Interpreted cross-section from the upstream channel trunk showing rotated block and debris flow fabrics of U1 and the interpreted channel elements, overbank deposits, and key seismic horizons (blue lines below C1 and C2 final channel elements). (C) Interpreted cross-section from the downstream channel trunk highlighting U5 and channels. Levee reflectors indicating typical active structural growth are indicated (based on Clark and Cartwright, 2011).

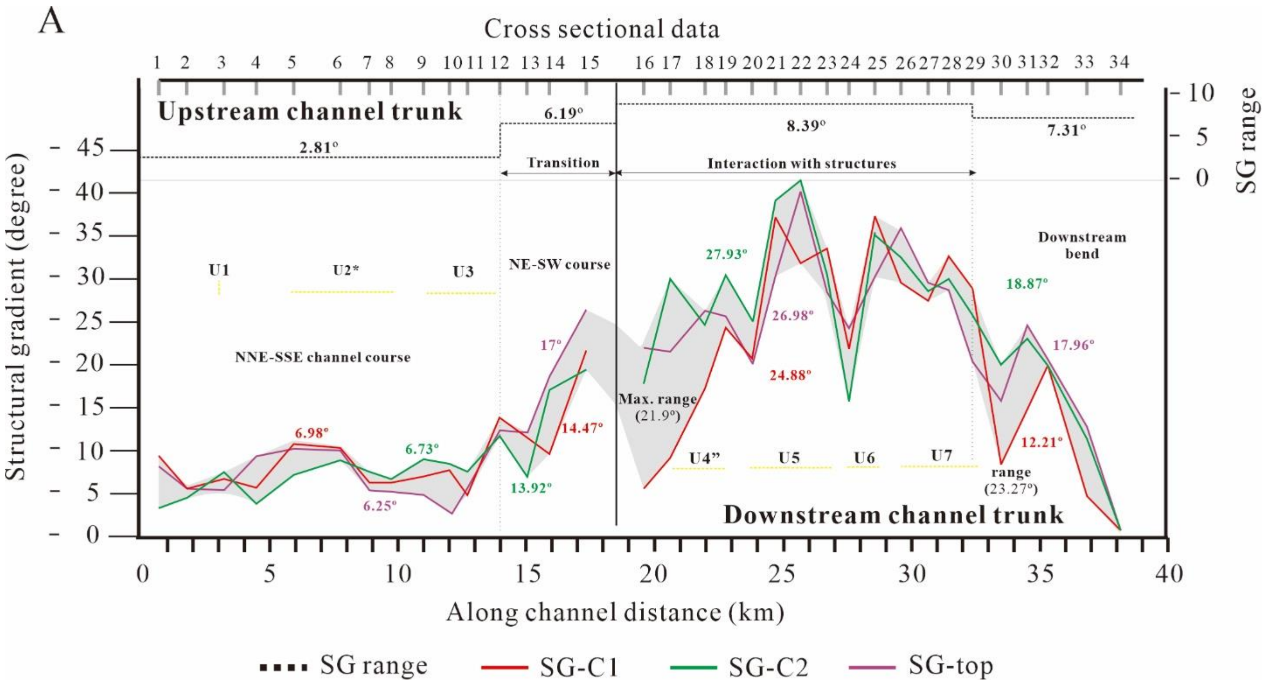

Figure 6. (A) Variation in structural gradients; SG-C1, SG-C2, and SG-top. Along channel distance was measured from the centerline of the Fulani Channel. Cross sectional data is indicated by positions of measurement points (see supplementary Material Fig. 1). Compartments of channel (upstream and downstream channel trunks) and zones of MTD interactions (U) are indicated along the Fulani Channel. The range extracted from different tilting of the youngest elements of channel complex C1, C2, and the top surface is shown in gray color, and plotted at the top with dashed black color line. The portion of the channel that interacted with structures' is indicated.

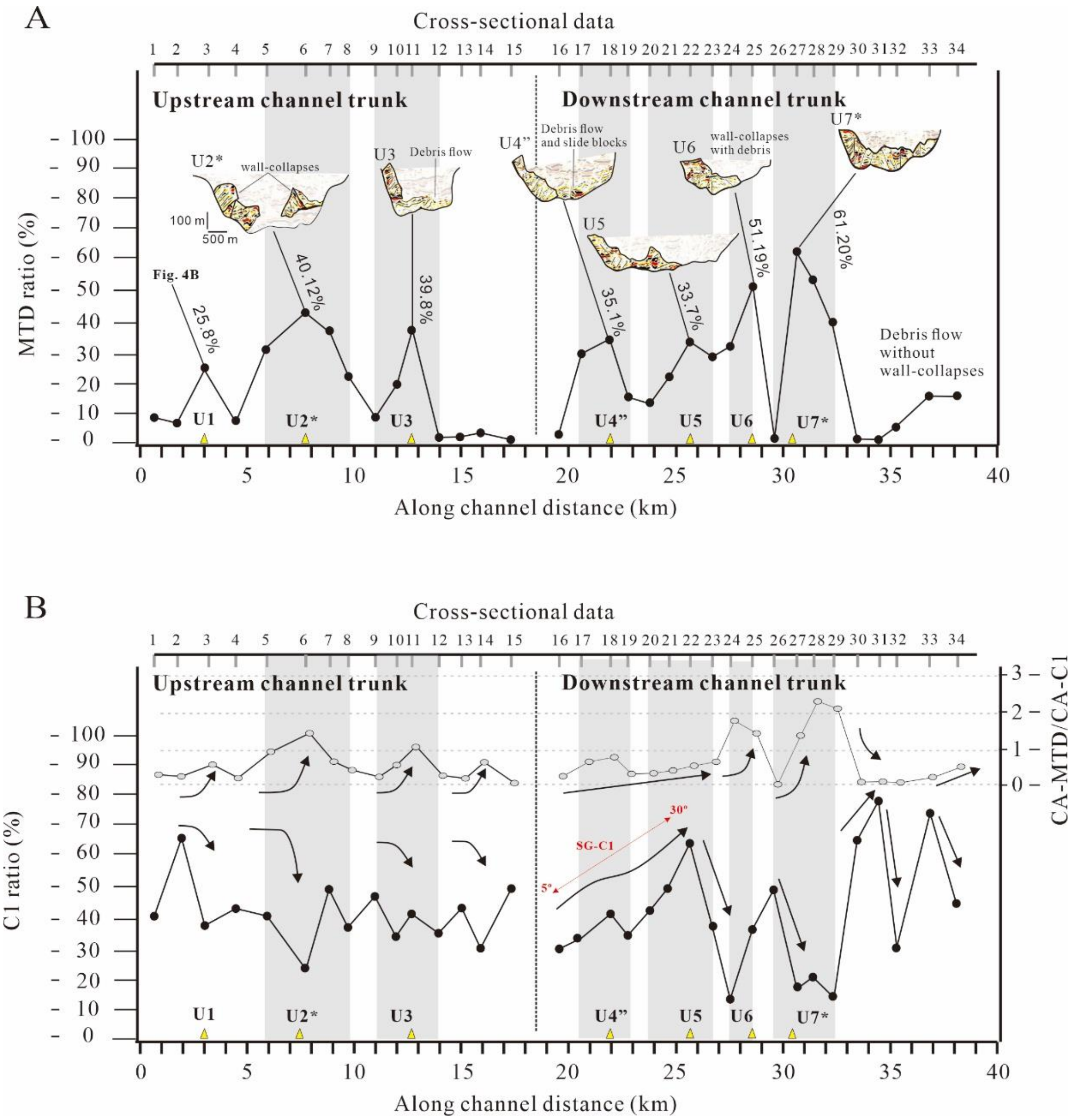

Figure 7. (A) Variation of MTD ratios along the channel, showing cross-sections at the key locations of each MTD unit (See Supplementary Material Fig. 3). (B) Variation of C1 ratio (i.e., the cross-sectional surface of channel complex C1 sedimentary fill normalized against the CA-Cb) along the channel distance (black) plotted with the relationships between MTD and C1 cross-sections (CA-MTD/CA-C1) indicated in gray. The channel compartments are indicated. Gray boxes represent the segments interacting with MTD. The red arrows indicate key location of SG-C1 variations around structures (Fig. 6). The asterisk (*) denotes multiple slide blocks (Sf4) distributed on both channel margins and double quotation (”) represents small slide blocks (Sf5) located in the channel bed.

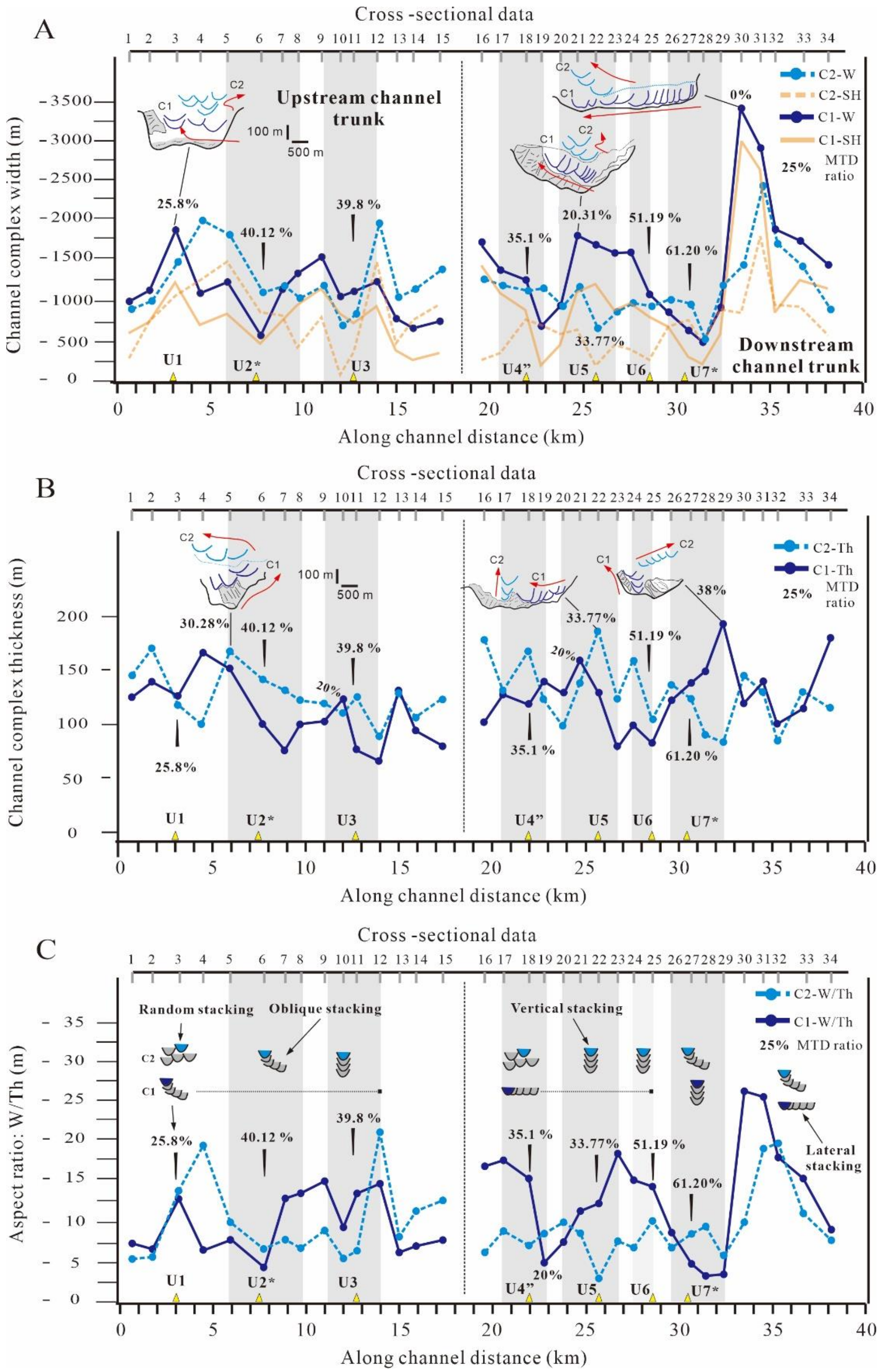

Figure 8. Downstream variation of channel complexes C1 (dark blue), and C2 (light blue). Lateral shift of C1 and C2 are indicated by orange line and dashed line, respectively. Illustrated cross-sections are indicated at key locations. (A) Width and lateral shift, (B) thickness, and (C) aspect ratio along the channel distance extracted from the centerline of the Fulani Channel belt. Channel compartments are indicated. Gray boxes

indicate the segments interacting with MTD units. Dominant style of cross-sectional stacking patterns is indicated for each channel complex.

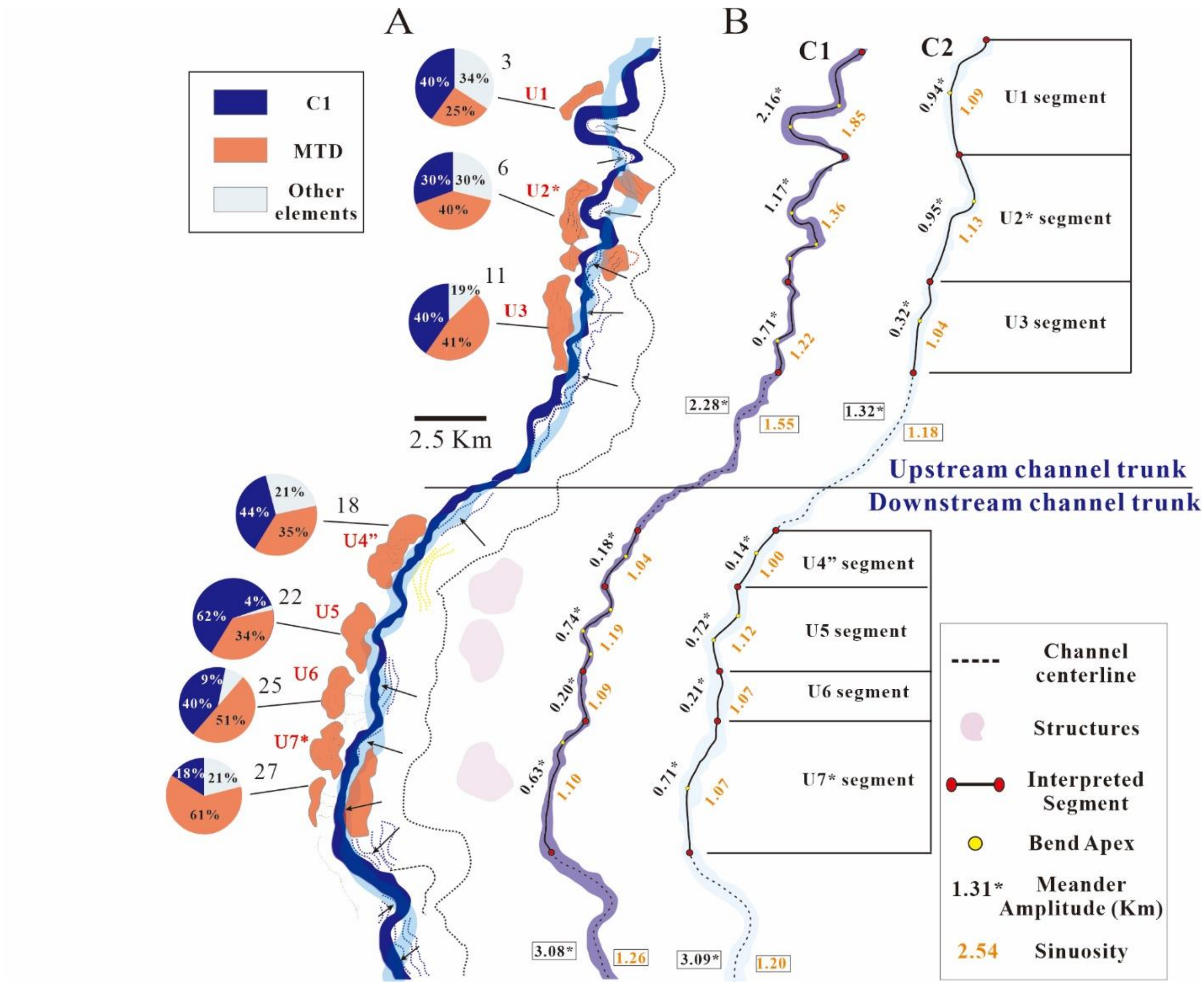

Figure 9. (A) Illustration of the planform distributions of C1 and C2 extracted from their respective variance maps (Fig. 1B and 5A). Percentages of MTD ratios (red), C1 ratios (dark blue), and other components of the channel base (e.g., internal levees, and aggradation low amplitude reflectors) are indicated at each unit. (B) Sinuosity and meander amplitude for each segment interacting with MTD (U segments), and at each compartment of the Fulani Channel (upstream and downstream channel trunks). Black arrows indicate the directions of lateral migration expressed by channel complexes.

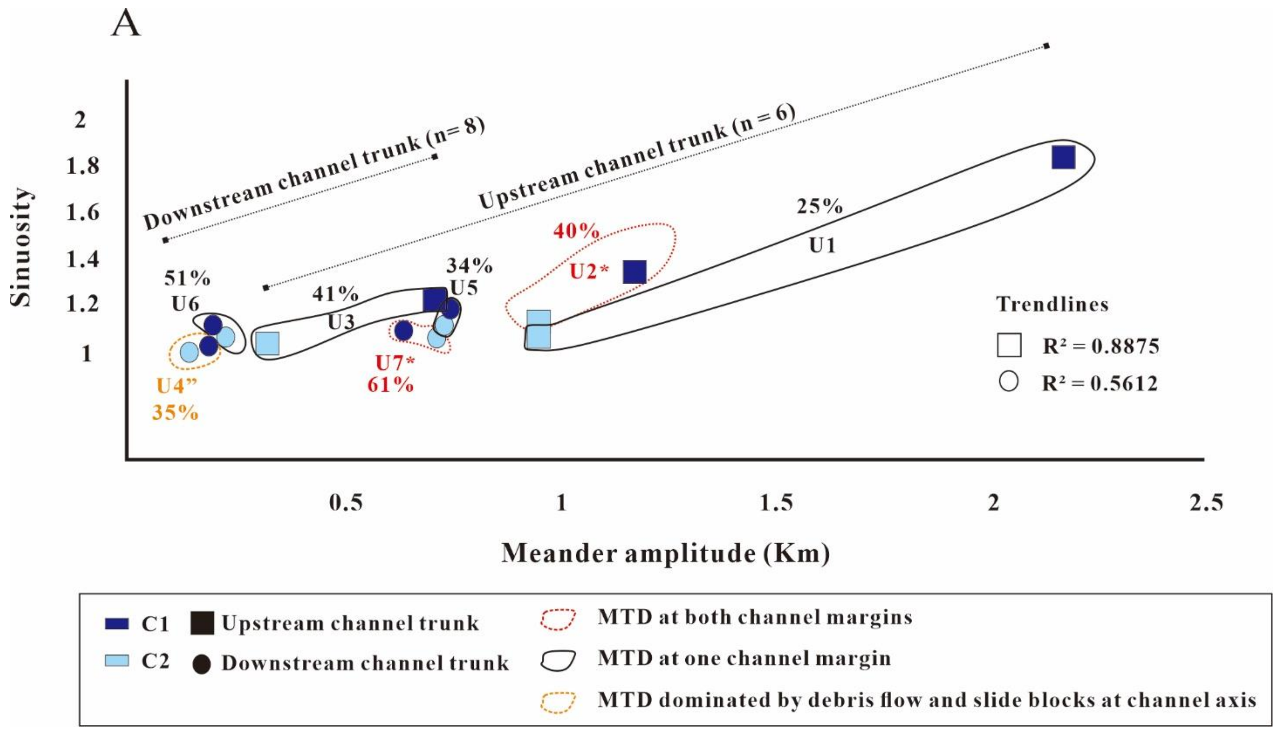

Figure 10. Sinuosity against meander amplitude for each U segment of Figure 9B, representing the channel complexes C1 (dark blue) and C2 (light blue). The segments from the downstream channel trunk range with lower sinuosity and amplitudes than the upstream channel trunk, all resulting linear increase with stronger correlation for the upstream sector. Wall-collapses distributed at both channel margins (red circle), and at one channel margin (black circle) demonstrate increase of planform parameters for decrease of MTD ratios. Wall-collapses dominated by slide blocks and debris flows at channel axis indicate very constrained planform parameters.

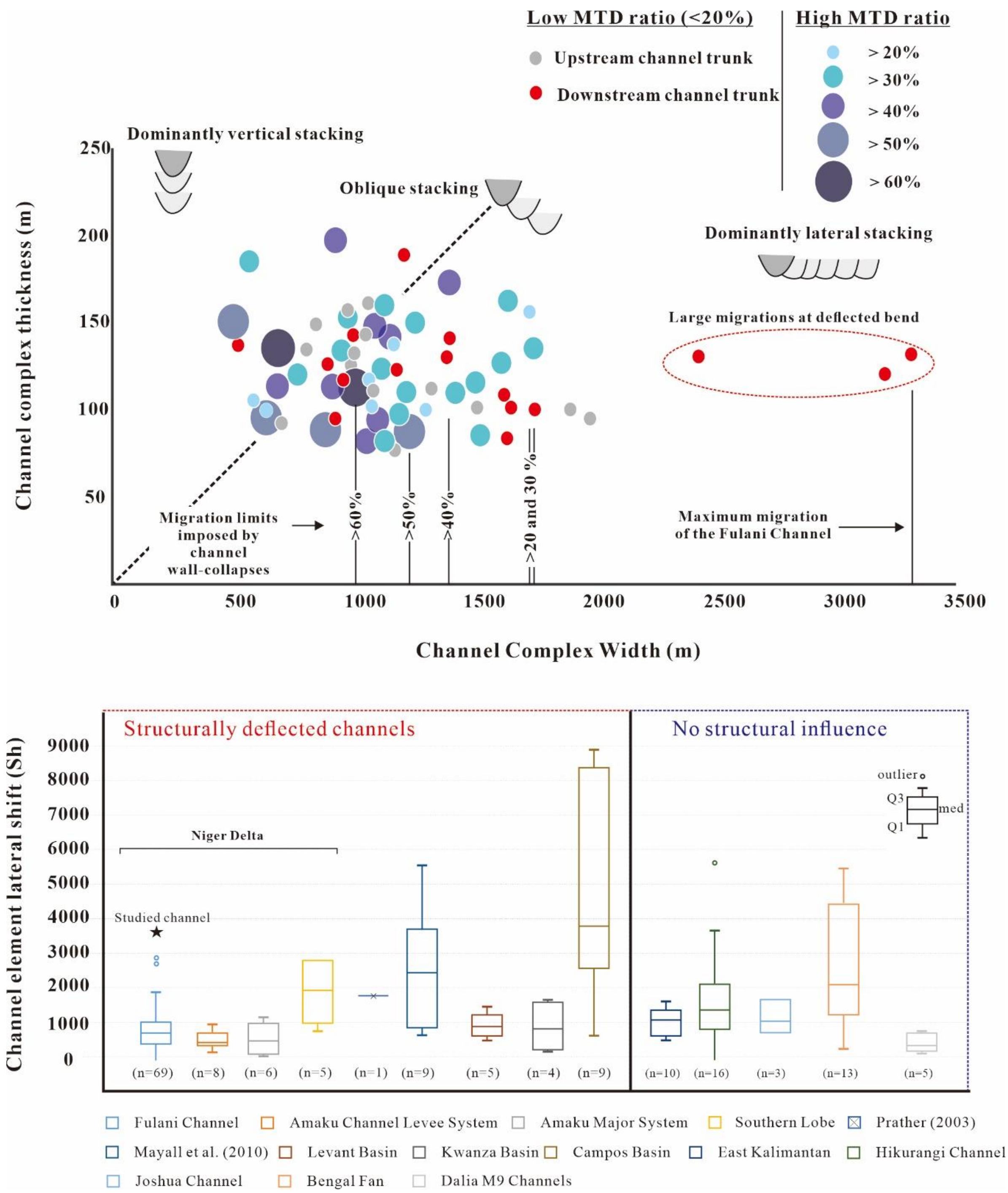

Figure 11. (A) Bubble plot of channel complex thickness against channel complex width of the Fulani Channel data. Lowest MTD ratios (<20%) are indicated for the unstructured upstream channel trunk (gray) and the deflected downstream channel trunk (red). High MTD ratios are indicated for >20% to >60% for both channel compartments. The dominant cross-sectional stacking patterns are robustly indicated. The lateral migration

limits (widths) are pointed for each MTD ratio. The migrations of the downstream deflected bend are indicated by a circle showing the extreme limit of channel migration in the study area. (B) Box-whisker plots for comparison of the lateral shift records of the studied channel with the global data sets of structurally deflected (e.g., Niger Delta, Nile Delta, offshore Angola, and Brazil) and non-structurally influenced channels (e.g., Indonesia, New Zealand, Gulf of Mexico, Bengal Fan, and offshore Angola). Campos basin channels (Covault et al., 2021) fall with highest Q3 values.